Article

Raman Fingerprints of the SARS-CoV-2 Delta Variant and Mechanisms of Its Instantaneous Inactivation by Silicon Nitride Bioceramics

Giuseppe Pezzotti,* Eriko Ohgitani, Yuki Fujita, Hayata Imamura, Masaharu Shin-Ya, Tetsuya Adachi, Toshiro Yamamoto, Narisato Kanamura, Elia Marin, Wenliang Zhu, Ichiro Nishimura, and Osam Mazda*

Read Online

ACCESS | Metrics & More | Article Recommendations | Supporting Information

ABSTRACT: Raman spectroscopy uncovered molecular scale markers of the viral structure of the SARS-CoV-2 Delta variant and related viral inactivation mechanisms at the biological interface with silicon nitride (Si_3N_4) bioceramics. A comparison of Raman spectra collected on the TY11-927 variant (lineage B.1.617.2; simply referred to as the Delta variant henceforth) with those of the JPN/TY/WK-521 variant (lineage B.1.617.1; referred to as the Kappa variant or simply as the Japanese isolate henceforth) revealed the occurrence of key mutations of the spike receptor together with profound structural differences in the molecular structure/symmetry of sulfur-containing amino acid and altered hydrophobic interactions of the tyrosine residue. Additionally, different vibrational fractions of RNA purines and pyrimidines and dissimilar protein secondary structures were also recorded. Despite mutations, hydrolytic reactions at the surface of silicon nitride (Si_3N_4) bioceramics induced instantaneous inactivation of

the Delta variant at the same rate as that of the Kappa variant. Contact between virions and micrometric Si_3N_4 particles yielded post-translational deimination of arginine spike residues, methionine sulfoxidation, tyrosine nitration, and oxidation of RNA purines to form formamidopyrimidines. Si_3N_4 bioceramics proved to be a safe and effective inorganic compound for instantaneous environmental sanitation.

KEYWORDS: SARS-CoV-2, delta variant, Raman spectroscopy, silicon nitride, instantaneous virus inactivation
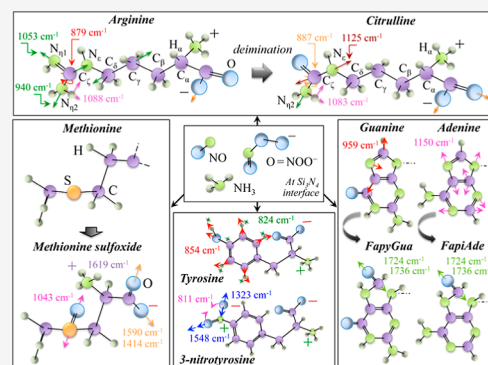
Surveys by the Japan's National Institute of Infectious Diseases confirmed that the highly transmissible SARS-CoV-2 Delta variant is presently the most widespread in Japan among confirmed cases.[1] Data from Tokyo and neighboring prefectures estimated that it exceeds 90% in each region, with similar rates in other Japanese prefectures with only a few exceptions. In other words, the Delta variant has almost entirely replaced the original SARS-CoV-2 Japanese isolate. Studies from Japan[2] and other countries[3,4] have shown a 2-fold infectious capacity of the Delta variant with respect to that of the Japanese isolate, with people infected with the Delta variant possessing a viral load more than 1200 times higher than that of people with the original SARS-CoV-2 isolate.[5] Among the numerous (at least 15) mutations of the Delta variant, those creating the most concerns are the two simultaneous ones referred to as E484Q and L452R;[6] the former contributes a significantly enhanced potential for binding to ACE2 and a better ability to evade the immune system, while the latter is instrumental in providing a higher affinity for the so-called "S" protein (prS) to ACE2 and in lowering the recognition capacity of the immune system.[7]

Notably, the appearance of both mutations in the same variant is unique so far.[8] Another mutation considered to be key is the one referred to as P681R, which transforms a proline residue in the furin cleavage site of the spike protein into an arginine one.[9] Hospitalization statistics unanimously point to a higher infectiousness of the Delta variant; concurrently, simulations show a transmissibility 145% higher than that of the original strain and a probability of infection approximately 2 times greater than that of the original isolate by droplet/aerosol inhalation.[10] So far, there is no definitive answer on the factors mainly contributing to such an increased degree of infectiousness, either a longer length of time the variant remains infectious in suspension or a higher activity is exhibited in fomite transmission.

In a recent paper,[11] we have shown the possibility of capturing fundamental details of the molecular structure and symmetry in different SARS-CoV-2 variants/sub-types by Raman spectroscopy. This spectroscopic method enables fast

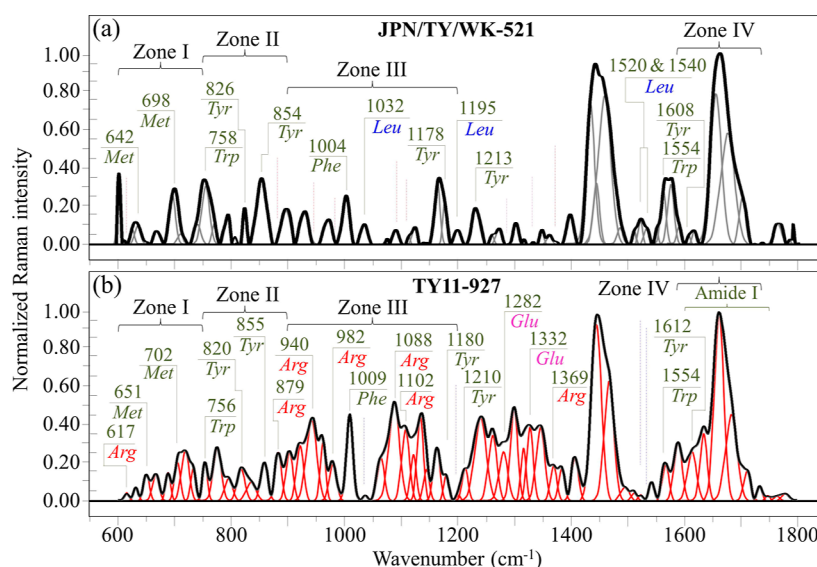**Figure 1.** Raman spectra in the wavenumber interval 600−1800 cm^{-1} of (a) JPN/TY/WK-521 and (b) TY11-927 Delta variants. Spectra are normalized with respect to the amide I signal and deconvoluted into Gaussian−Lorentzian band components according to eq 1 in the Methods section. Four zones are emphasized in (a), and labels show frequencies at the maximum of selected bands (the abbreviations *Met, Tyr, Phe, Leu, Arg,* and *Glu* stand for methionine, tyrosine, phenylalanine, leucine, arginine, and glutamine, respectively).

screening and, complementary to genomics, brings insightful structural information of amino acid residues, RNA bases, and the secondary protein structure of virions. The differences in the molecular structure and symmetry between the SARS-CoV-2 Japanese isolate and the two sub-types of the Alpha variant were stunningly bold. In two additional studies,[12,13] we have proposed the exploitation of the surface chemistry of silicon nitride bioceramics in an aqueous environment as an instantaneous and powerful antiviral effect against SARS-CoV-2. Unlike other solid-state antiviral agents,[14] Si_3N_4 is a compound fully biocompatible toward eukaryotic cells while effectively countering pathogens.[15−18] Such duality is the result of its peculiar surface chemistry, which features a cell-supportive cation (silicon) and the formation of ammonia/ammonium (and nitrogen radicals) as byproducts of hydrolytic interaction between surface secondary amines and the aqueous environment at the biological interface.[15,16] Eukaryotic cells and pathogens greatly differ in their capacity of metabolizing un-ionized species of ammonia, which originates the observed "antibiotic-like" behavior of Si_3N_4. Since ssRNA virions have no capacity to resist ammonia attack to their RNA and viral proteins,[19,20] they become instantaneously inactivated by the presence of a few volume percent of micrometer-sized Si_3N_4 particles in aqueous solution.[12,13,15]

This paper builds upon our previous studies of the SARS-CoV-2 virus with a new twofold purpose: (i) to extend the Raman spectroscopic identification of the virus to the Delta variant (TY11-927) found in Japan, as distinct from the Japanese Kappa isolate, and (ii) to test the viral inactivation activity of the Si_3N_4 micrometric powder against the Delta variant, while delving into the molecular chemistry mechanisms behind its instantaneous inactivation pathway. Accordingly, we focus here on the confirmation of a direct link between Raman light and key structure/symmetry characteristics of virions' molecular structure as chemical fingerprints for different variants and degenerative effects on SARS-CoV-2 virions.

■ RESULTS

Raman Spectrum of the SARS-CoV-2 Delta Variant and Its Statistical Reliability. Figure 1a,b shows the Raman spectra (i.e., average of 10 spectra collected at different locations) measured on the Kappa JPN/TY/WK-521 and Delta TY11-927 variants, respectively. It can immediately be noticed that the two average spectra appear morphologically very different to each other. Such differences were screened for statistical reliability according to the Pearson's similarity method,[21] as described in the Methods section. Results of the statistical analyses that validate the average spectral morphology of the two different variants are given in Table 1 in terms of the PC coefficient, r (cf. explanation in the

Table 1. Results of the Statistical Analysis to Validate the Average Spectral Morphology of the Two Studied Variants According to Pearson's Correlation Coefficient (PC), r

	JPN/TY/WK-521	TY11-927
JPN/TY/WK-521	0.925 ± 0.065	0.498 ± 0.83
TY11-927	0.576 ± 0.097	0.899 ± 0.113

Methods section). As seen, when compared to their average spectrum, individual spectra collected on the Delta variant at different sample locations showed an r value close to 1 with a small data scatter ($r = 0.899 \pm 0.113$). On the other hand, the value of the r coefficient significantly reduced to 0.576 ± 0.097 when they were compared to the JPN/TY/WK-521 average spectrum. Similarly, when individual spectra collected at different locations on the JPN/TY/WK-521 sample were compared to their average spectrum and the average TY11-927 spectrum, they displayed values of $r = 0.925 \pm 0.065$ and 0.498 ± 0.83, respectively. The presented statistical results of spectral similarity according to the Pearson's method are in agreement with our previous data on SARS-CoV-2 British variants[11] and demonstrate the high sensitivity for the Raman approach in SARS-CoV-2 viral speciation. Four frequency intervals of the Raman spectra, labeled as zones I−IV in the inset to Figure 1a

(at 600−750, 750−900, 900−1200, and 1600−1750 cm^{-1}, respectively), were analyzed in detail. Average spectra were normalized with respect to their amide II signal at 1460 cm^{-1} and deconvoluted into band components according to a machine learning algorithm described in the Methods section. A complete list of frequencies at the maximum and their proposed vibrational origins has been given in a previous publication.[11]

Raman Signatures Linked to Virus Mutations. A number of the observed spectral differences between variants are expected to arise from amino acids, which are linked to specific mutations of the Delta variant (cf. mutations reported for the spike protein of the TY11-927 (B.1.617.2) variant in Table 2). Among the reported mutations, the E484Q one

Table 2. Mutations Reported for the Spike Protein of the TY11-927 (B.1.617.2) Variant[6,9]

spike protein mutations	position	description
T19R	19	threonine-to-arginine substitution
G142D	142	glycine-to-aspartic acid substitution
Δ156−157	156−157	deletion
R158G	158	arginine-to-glycine substitution
Δ213−214	213−214	deletion
L452R	452	leucine-to-arginine substitution
T478K	478	threonine-to-lysine substitution
D614G	614	aspartic acid-to-glycine substitution
P681R	681	proline-to-arginine substitution
D950N	950	aspartic acid to asparagine substitution

foresees the change from glutamic acid into glutamine, while the L452R one relates to the replacement of leucine by arginine.[6] An additional mutation, referred to as P681R, transforms a proline residue in the furin cleavage site of the spike protein into an arginine one.[9] According to the above

notions, we looked first into specific spectral fingerprints of the arginine residue to replace those from the leucine one in the spectrum of the TY11-927 Delta variant as compared to that of the JPN/TY/WK-521 original isolate. The main bands assigned to leucine and arginine residues are labeled in Figure 1a,b, respectively, as obtained from the spectra of their pure compounds (in Figure S1a,b of the Supporting Information, respectively). The machine learning algorithm used in this study (cf. the Methods section), which picked from a library of pure compounds, located prominent spectral contributions assignable to the basic arginine amino acid residue in the spectrum of the Delta variant at 617 cm^{-1} (COH bending), 879 cm^{-1} (C−N torsion), 940 and 982 cm^{-1} (N−C−N symmetric stretching), 1088 cm^{-1} (C−N−H$_2$ asymmetric bending), 1102 cm^{-1} (NH$_3^+$ asymmetric rocking), and 1369 cm^{-1} (COO$^-$ symmetric stretching) (cf. the structure, Raman spectrum of the arginine pure compound, and assignments of the main fingerprint vibrational modes given in Figure S1b).[22−24] All these Raman signals were either missing or very weak in the spectrum of the Japanese Kappa isolate (cf. Figure 1a,b). Concurrently, we analyzed signals from leucine (cf. the structure, Raman spectrum of the leucine pure compound, and related assignments of fingerprint vibrational modes given in Figure S1a of the Supporting Information)[22] and labeled them, as shown in Figure 1a. Fingerprint leucine signals, which do not overlap with signals from other amino acid residues, could be located at 1032 cm^{-1} (C−N stretching), 1195 cm^{-1} (NH$_3^+$ asymmetric rocking), 1520 cm^{-1} (NH$_2$ asymmetric stretching and rocking), and 1540 cm^{-1} (CH$_3$ symmetric bending).[22,25−27] All these signals were indeed detected in the Raman spectrum of the JPN/TY/WK-521 original isolate but were conspicuously weaker in that of the TY11-927 Delta variant.

Regarding the E484Q mutation, we performed the machine learning algorithm searching for vibrational fingerprints of glutamic acid and glutamate. The structures of these two
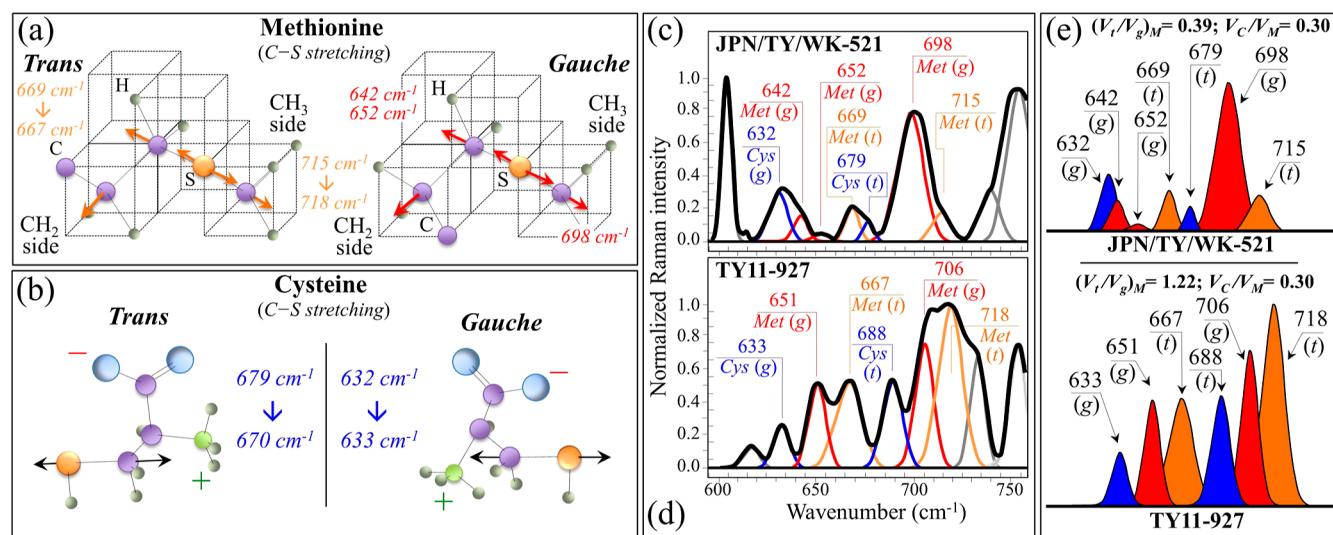
Figure 2. (a) Structures and C−S stretching vibrational modes/frequencies of *trans* and *gauche* methionine rotamers and (b) *gauche* and *trans* rotamers of cysteine with C−S stretching vibrational modes/frequencies. Low-frequency zone I (600−750 cm^{-1}) regions of the Raman spectra of JPN/TY/WK-521 and TY11-927 viral strains are given in (c,d), respectively, spectra were deconvoluted into a sequence of Gaussian−Lorentzian sub-bands (frequencies for selected bands are shown in the inset). The abbreviations *Met* and *Cys* refer to methionine and cysteine, respectively, while (*t*) and (*g*) locate *trans* and *gauche* rotamers, respectively. In (e), sub-band components are extracted to better visualize signals from different rotameric configurations of the methionine structure (the related methionine *trans*-to-*gauche*, $(V_t/V_g)_M$, and the cysteine-to-methionine, V_C/V_M, ratios are given in the inset together with labels of band wavenumbers and types of the rotamer).
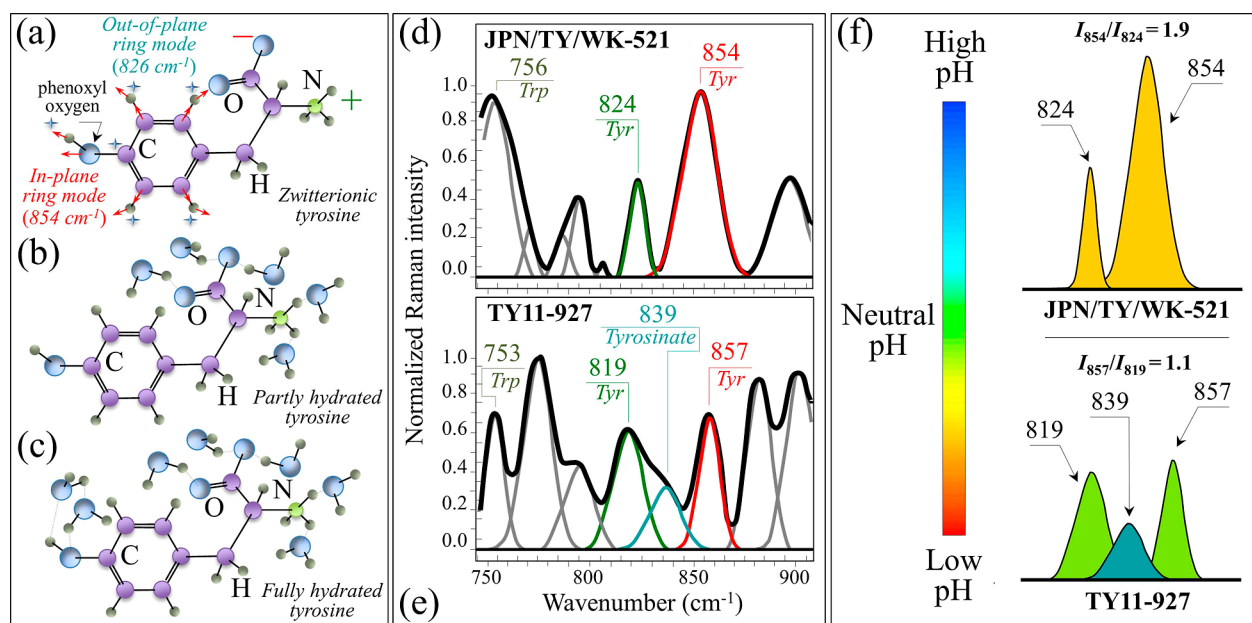
Figure 3. Structure of tyrosine in (a) zwitterionic, (b) non-hydrated, and (c) fully hydrated conditions are shown together with in-plane and out-of-plane vibrational modes of the phenol ring according to ref 43. Spectral zone II (750−900 cm^{-1}) of the Raman spectra of (d) JPN/TY/WK-521 and (e) TY11-927 viral strains; spectra are deconvoluted into a sequence of Gaussian−Lorentzian sub-bands (frequencies for selected bands shown in the inset). The abbreviations *Trp* and *Tyr* refer to tryptophan and tyrosine, respectively. In (f), tyrosine sub-band components are shown together with the Raman ratio, I_{854}/I_{826} (cf. labels in the inset and a qualitative estimate of the environmental pH at the surface of different viral strains).

compounds, their Raman spectra, and related assignments of fingerprint vibrational modes are given in Figure S2a,b, respectively, of the Supporting Information.[28−31] Two unequivocal fingerprints of glutamine could be located in the signals at 1282 cm^{-1} (CH$_2$ wagging) and 1332 cm^{-1} (CH bending), which were observed as being relatively strong in the TY11-927 variant while being very weak or completely missing in the JPN/TY/WK-521 isolate (cf. Figure 1a,b).

Finally, a further bold spectral difference between JPN/TY/WK-521 and TY11-927 variants consisted in the disappearance in the latter of a sharp feature of medium intensity at ∼604 cm^{-1}. Lysine possesses such a signal, which is related to asymmetric bending of its NH$_3^+$ group.[22] Lysine-to-asparagine substitution has been reported in some sequence of the Delta variant and has been associated with conformal changes in the spike protein, which might favor immune escape.[32] However, we could not find in the spectrum any other unequivocal confirmation for the disappearance of additional lysine bands due to overlapping with other signals.

Spectroscopic Analyses in Selected Spectral Zones. Zone I—Figure 2a,b shows the schematic drafts of methionine (Met) and cysteine (Cys), respectively. *Trans* (*t*) and *gauche* (*g*) rotamers appear at different wavenumbers in spectral zone I, according to the vibrational modes shown in the inset. Spectra in (c and d) represent the Raman low frequency zone I as recorded for JPN/TY/WK-521 and TY11-927 viral strains, respectively. This zone, which is dominated by vibrational signals relating to the C−S bond,[22] allows monitoring methionine and cysteine amino acid residues incorporated into viral proteins. Raman assessments in this spectral zone show significant differences between variants, which arise from both fractions and molecular symmetry of S-containing amino acid residues. In the JPN/TY/WK-521 original isolate, C−S stretching bands from methionine residues are found at 642

and 652 cm^{-1} (C−S bond stretching vibrations on the CH$_2$ side of molecules in the gauche rotameric configuration), 669 cm^{-1} (C−S bond stretching vibrations on the CH$_2$ side of molecules in the trans rotameric configuration), 698 cm^{-1} (C−S stretching on the CH$_3$ carboxyl side in the gauche configuration), and 715 cm^{-1} (C−S stretching on the CH$_3$ carboxyl side in the trans configuration) (cf. insets in Figure 2a).[33,34] In the TY11-927 variant, the C−S bond-related Raman bands show both distinct shifts in the wavenumber and bold variations in their relative intensities as compared with that of the original isolate (cf. labels in the inset to Figure 2a, spectra in Figure 2c,d, and sub-bands replotted in Figure 2e). In particular, an enhancement of the signal at 651 cm^{-1} was observed, while the companion signal at 642 cm^{-1} was too weak to be detectable. Differences in the fractions of methionine rotamers are a consequence of the different amino acid sequences to which methionine links,[11] and different molecular symmetry characteristics are expected to play a key role in a number of functions during the virus lifetime.[35,36] The methionine *trans*-to-gauche ratios, $(V_t/V_g)_M$, were computed from the relative areal fractions of C−S bonds to be 0.39 and 1.22 for JPN/TY/WK-521 and TY11-927, respectively (cf. labels in the inset to Figure 2e). These different ratios reflect chirality characteristics peculiar to individual strains and can be used as efficient fingerprints in variant recognition. Similar to the case of methionine, the C−S stretching wavenumbers of zwitterionic (monoclinic) cysteine rotamers also differed for different variants (cf. Figure 2b−d).[37−40] The C−S stretching bands, found at ∼632 and ∼679 cm^{-1} in the JPN/TY/WK-521 isolate for gauche and trans rotamers, respectively (cf. Figure 2c), shifted to 633 and 688 cm^{-1}, respectively, and showed inverted relative intensities in the TY11-927 variant (cf. Figure 2d). However, the ratio between the cumulative areal fractions of cysteine and
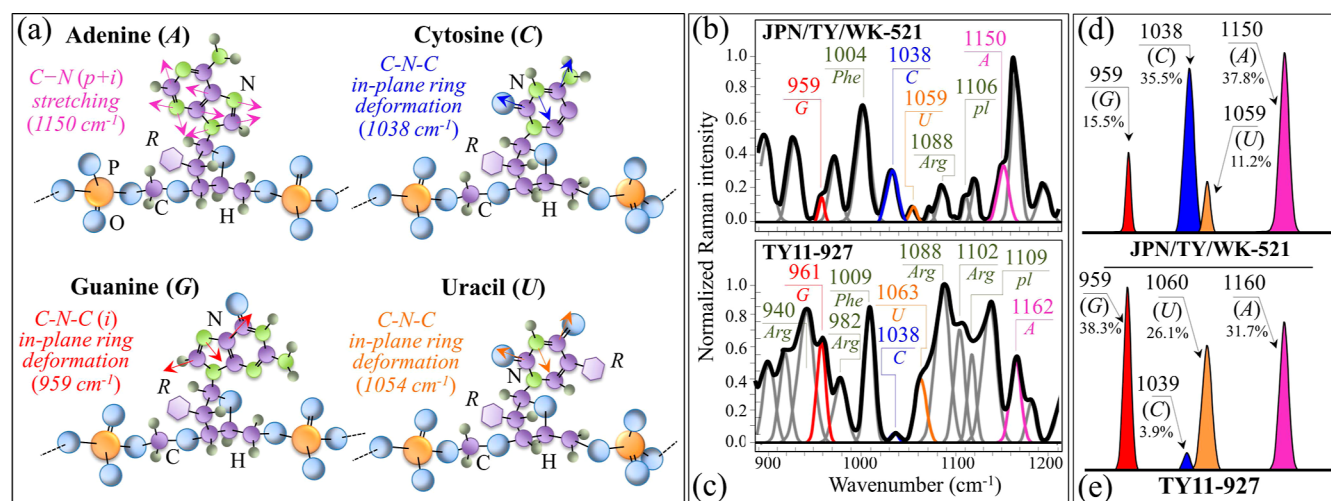
Figure 4. (a) Schematic draft of purines and pyrimidines with phosphodiester linkages together with the ring vibrational modes selected to locate different RNA bases (abbreviations p and i in brackets refer to pyridine and imidazole rings, respectively). Spectral zone III (900−1200 cm^{-1}) is given in (b,c) for the Raman spectra of JPN/TY/WK-521 and TY11-927 viral strains, respectively; spectra are deconvoluted into a sequence of Gaussian−Lorentzian sub-bands (wavenumbers for selected bands shown in the inset). The abbreviations G, C, U, pl, and A refer to guanine, cytosine, uracil, phosphodiester linkages, and adenosine, respectively; in (d,e), sub-band signals are separately shown and used to estimate the fractions of different purine and pyrimidines (shown in the inset together with the wavenumbers of the selected signals) found in different strains.

methionine bands remained unchanged in the two viral strains (i.e., $V_C/V_M = 0.3$; cf. insets in Figure 2e). Unlike the strongly hydrophobic methionine unequivocally located at buried sites in the core of globular proteins, cysteine is exposed to the surface and its thiol side chain participates as a nucleophile in environmental reactions (being also susceptible to oxidation). For this reason, the cysteine signals sense different pH environments at the virion surface, as discussed later.

Zone II—Figure 3a−c shows the schematic drafts of the molecular structure of tyrosine with different degrees of hydration. Vibrations of its phenol ring "feel" the surrounding environment, the relative intensity of the so-called tyrosine Fermi doublet (found at 854/824 and 857/819 cm^{-1}) in the spectra of JPN/TY/WK-521 and TY11-927, respectively (Figure 3d,e), enabling the analysis of virion/environment interactions. The intensity ratio, I_{854}/I_{826}, is diagnostic of the H-bonding environment around the tyrosine units, and the lower the ratio, the more hydrophobic the surrounding environment.[41−43] The ratio differed significantly in different strains (i.e., 1.9 and 1.1 for JPN/TY/WK-521 and TY11-927 variants, respectively; cf. labels in Figure 3f). According to Hernandez et al.,[43] the components of the tyrosine doublet originate from two independent vibrational modes of the phenol ring, namely, in-plane ring breathing (854 cm^{-1}) and out-of-plane C−H bending (826 cm^{-1}). The I_{854}/I_{826} ratio is a sensor of the hydrophobic/hydrophilic balance in environmental interactions at the virion surface, and the lower the I_{854}/I_{826} ratio, the more hydrophobic the tyrosine configuration. Since tyrosine is the most hydrophobic in an alkaline environment (and vice versa for the acidic environment), the lowered I_{854}/I_{826} intensity ratio observed in the Delta variant as compared to that in the Kappa variant (i.e., 1.1 vs 1.9, respectively) proves that the Delta variant has shifted its surface protonation conditions toward alkaline (and more hydrophobic) ones. Following the analysis by Arp et al.[44] the enhanced character of the hydrogen bond donor to the tyrosine phenoxyl proton in the TY11-927 variant contrasts with the prevalently acceptor character of the tyrosine phenoxyl oxygen in the original JPN/TY/WK-521 virions.

Additional spectral features were found that substantiate the above analysis. Following previous studies of filamentous viruses,[45,46] a pH increase alters the morphology of the Raman tyrosine doublet with the new appearance of a relatively strong band at ∼839 cm^{-1} (i.e., between the doublet) and a weak band at 812 cm^{-1}. In the spectrum of the Delta variant, the former signal could clearly be detected, while the latter one was too weak and overlapped to be resolvable (cf. Figure 3e,f). This spectral characteristic suggests the coexistence of tyrosine and tyrosinate moieties in the protein structure of the Delta variant. Indeed, the value of the I_{857}/I_{819} intensity ratio observed in this variant (i.e., 1.1) nears the intermediate value (i.e., ∼1.25) usually reported in the literature for the phenolic OH group acting as both the donor and acceptor of moderate hydrogen bonds.[47] A tendency to deprotonation is symptomatic of an increased environmental pH and agrees with the finding of a lowered tyrosine intensity ratio. A further confirmation that corroborates the tyrosine doublet trend in the TY11-927 spectrum is the appearance of a low-wavenumber amide I signal at 1635 cm^{-1} (cf. Figure 1a,b), which is also a marker of environmental pH enhancement around tyrosine (cf. additional discussion later in this section).[43] The lowered tyrosine doublet ratio and the 839 cm^{-1} signal of tyrosinate are markers of an altered virion/environment equilibrium in the Delta variant. Finally, note also that zone II contains the breathing vibration of the indole ring of tryptophan at 753−756 cm^{-1} (cf. Figure 3a,b). This latter vibration is ∼20% lower in the Delta variant than in the Kappa one. A comparison of key residues in SARS-CoV-2 variants by Deval et al.[48] has shown that tryptophan was the most common residue in both Delta and Kappa variants. This notion was confirmed by the Raman data shown in this study in comparison with the spectra of two Alpha sub-variants shown in a previously published work.[11]

Zone III—Figure 4a shows the structure of RNA bases and the fingerprint Raman signals by which they can be located in the spectrum of viruses. The in-plane deformations of C−N−C bonds in the heterocyclic aromatic ring of cytosine (C) and uracil (U) pyrimidines are displayed at different wavenumbers (i.e., at 1038 and 1054 cm^{-1}, respectively)[49−52] because
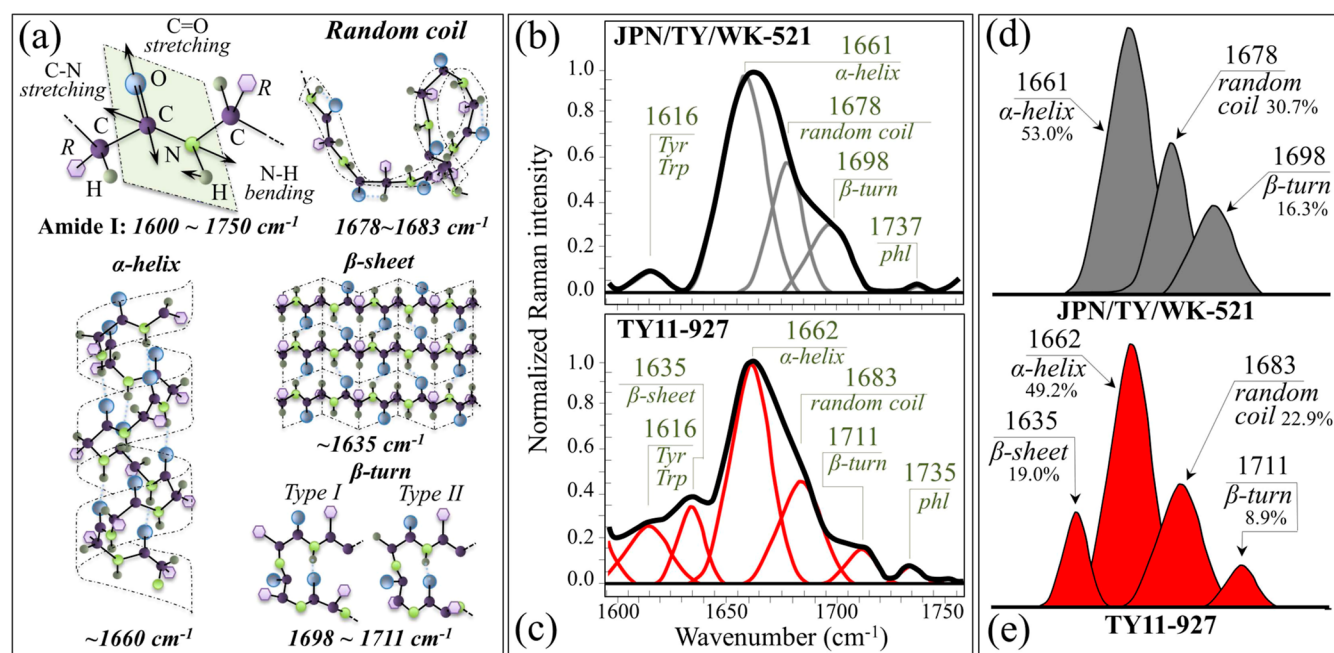
Figure 5. (a) Schematic drafts of the amide I vibrational mode, the different secondary structures of proteins and their related wavenumbers. Spectral zone IV (amide I, 1600−1750 cm^{-1}) of the Raman spectra of (b) JPN/TY/WK-521 and (c) TY11-927 viral strains; spectra were deconvoluted into a sequence of Gaussian−Lorentzian sub-bands (wavenumbers for selected bands shown in the inset). In (d,e), signals are shown and used to estimate the fractions of different protein secondary structures (shown in the inset together with the wavenumbers of the selected signals) found in different strains. The abbreviations *Tyr*, *Trp*, and *phl* represent tyrosine, tryptophan, and phospholipids, respectively.

different functional groups are attached to their six-membered pyrimidine ring. The same C−N−C vibration in the five-membered imidazole ring of guanine (G) purine appears at a significantly lower wavenumber (i.e., 959 cm^{-1}) as a consequence of the different structure of the ring.[51,52] On the other hand, a cumulative signal from C−N stretching in both five-membered imidazole and six-membered pyrimidine rings of the adenine (A) purine is displayed at 1150 cm^{-1}.[51,53] Figure 4d,e summarizes the differences in relative intensity of signals from purines and pyrimidines in the two investigated strains. In the inset, fractional intensity values are shown, as computed by assuming the sum of selected signals from all purine and pyrimidine bases to be 100%. These fractional differences capture the process of genome "reshuffling" occurred in the Delta variant. However, the RNA "Raman fractions" usually do not match those obtained by genome analyses[11] because they are altered by base pairing, signal cross-sections, and the presence of viral nucleoproteins associated at preferential RNA sites.[54] Besides vibrational signals from RNA bases, zone III also contains signals peculiar to phenylalanine at ∼1004 cm^{-1} (symmetric ring breathing), phosphodiester linkages of the RNA backbone (*pl* band) at 1106−1109 cm^{-1},[55] and arginine at 940, 982, 1088, and 1102 cm^{-1} (cf. previous section) (cf. labels in Figure 4b,c). The relative intensity of the *pl* band, which is proportional to the number of nucleotides units of ordered structures (and thus gives the number of nucleotides involved in secondary interactions), is 3 times higher in the spectrum of the Delta variant. This means that the Delta variant presents a much higher probability of secondary interaction than the original isolate. Regarding the four arginine signals, as discussed in the previous section, they appear to be peculiar to the Delta variant except for the band at 1088 cm^{-1}, which shows a weaker signal

also in the spectrum of the original isolate (likely contributed by other molecules).

Zone IV—Figure 5a shows schematic drafts of the secondary structures of proteins and their expected ranges of vibrational (amide I) frequencies: signals at ∼1635, ∼1660, 1678−1683, and 1698−1711 cm^{-1} represent secondary structures of the β-sheet, α-helix, random coil, and two β-turn rotamers (type I and type II), respectively.[54] Deconvoluted Raman spectra in the amide I region (1600−1750 cm^{-1}) of the JPN/TY/WK-521 and TY11-927 variants are given in Figure 5b,c, respectively. In the deconvoluting signals related to the protein secondary structure, machine learning training was performed according to the work of Maiti et al.[56] In Figure 5d, amide I signals are extracted from the respective deconvoluted spectra and compared for different isolates (cf. labels). A common feature resided in the predominance of the α-helix component in both investigated viral strains. However, the amide I spectra of the Delta variant was clearly different from that of the Japanese Kappa isolate, reflecting a substantial dissimilarity in the protein secondary structure between the two strains. The most striking difference was the lack of the β-sheet signal in the JPN/TY/WK-521 strain, coupled to the absence of a signal from the β-turn type II rotamer (cf. Figure 5b,c). Both these signals were instead clearly detected in the spectrum of the Delta variant. Fractional amounts of protein secondary structures were computed from the relative intensities of the amide I spectrum, as shown in the inset to Figure 5d,e. According to a Raman study of proteins in an aqueous environment published by Eker et al.,[57] a hydrophobic environment leads to a propensity to form the β-sheet structure. The present results agree with this trend since the Delta variant experienced a lowered I_{854}/I_{826} tyrosine ratio (i.e., a marker of increased environmental hydrophobicity and increased pH) as compared to the Kappa variant. Recent cryo-

electron microscopy analyses of the conformational states of the Delta spike have shown that the Delta T478K substitution (cf. Table 2) plays a fundamental role in stabilizing and reshaping the receptor-binding domain, enhancing the interaction with the host-cell receptor ACE2.[58] Using a similar approach, Yurkovetskiy et al.[59] showed how D614G changes affect the conformation of the S1 domain in the SARS-CoV-2 spike; the association rate between D614G and ACE2 being slower than that between D614 and ACE2 and the dissociation rate of D614G being faster and resulting in a lower affinity. In silico studies by Calcagnile et al.[60] predicted that D614G replacement could drastically change the peptide secondary structure by replacing the (intracellular) C-terminal β-sheet with the α-helix in the region close to the mutation with a consequent increase in flexibility and variations in affinity between ACE2 and the D614G spike. However, unlike the T478K mutation, the D614G mutation is peculiar to both variants studied here.[61] Accordingly, it is difficult to directly link the observed conformational differences to a specific mutation using Raman spectroscopy. Since the spike protein needs to be in an open-state conformation to interact with ACE2 and initiate viral entry,[62] the present Raman study suggests that the increase in infectivity reported for the Delta variant could be linked to a higher propensity of its spike proteins to unfold or to spend more conformational time in the open form as a consequence of the enhanced alkalinity of its surface environment.

Raman Barcodes. In a previous report,[11] we proposed to identify different SARS-CoV-2 variants by constructing a barcode from their deconvoluted (average) Raman spectra. Each line of the barcode has a thickness equal to 1/50 of the deconvoluted sub-band width and a distance from the successive line proportional to the sub-band area. We suggested that once the Raman technology could be refined to allow prompt on-site analyses, the Raman barcode could enable efficient electronic recordkeeping and increase users' accessibility to both emergence and transmission characteristics of variants through apps and user-friendly software. Figure 6 shows Raman barcodes for the JPN/TY/WK-521 and TY11-927 variants, as constructed from their deconvoluted Gaussian−Lorentzian sub-bands (replotted from Figure 1). For comparison, deconvoluted sub-band components and Raman barcodes are also shown for the two British variants QK002 and QHN001 investigated in ref 11. As seen, the obtained Raman barcodes were capable of unambiguously locating all virus variants. Similar to the recently proposed "genetic barcode" (based on genetic data extracted from coronavirus tests according to a global genome database),[63] the "Raman barcode" is capable of locating the multiplicity of slightly different versions of the virus among infected people within their general classification into individual variants, likely using an analytical procedure less cumbersome than genomic sequencing.

Inactivation of the SARS-CoV-2 Delta Variant by Si_3N_4 Bioceramics. Figure 7 summarizes a set of immunochemistry evidence pieces demonstrating the antiviral effect of Si_3N_4 powder against SARS-CoV-2 JPN/TY/WK-521 and TY11-927 virions were exposed to a 5 vol % Si_3N_4 powder-containing aqueous solution. Figure 7a,b shows the fragmentation of viral RNA upon 1 min exposure to the aqueous suspension, as evaluated by means of reverse transcription polymerase chain reaction (RT-PCR) analyses on the N-gene sequences of Kappa and Delta variants, respectively. Both supernatant
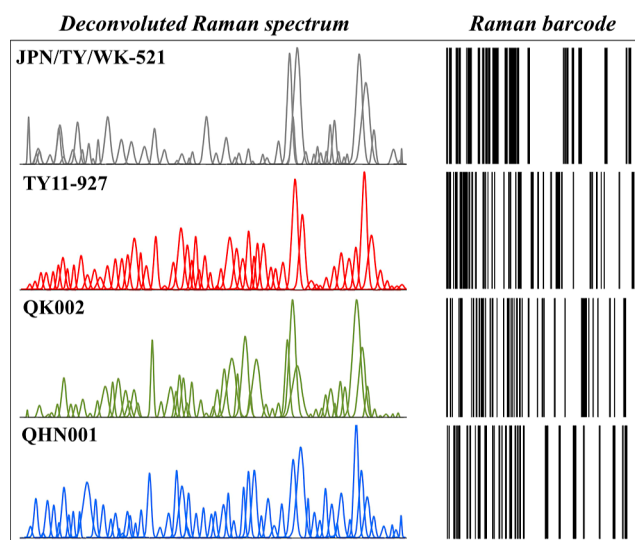

Figure 6. Sequences of Gaussian−Lorentzian deconvoluted sub-bands and related Raman barcodes for the Kappa JPN/TY/WK-521 and Delta TY11-927 variants are compared to those of two previously reported British variants QK001 and QHN001 (from ref 11; cf. labels in the inset).
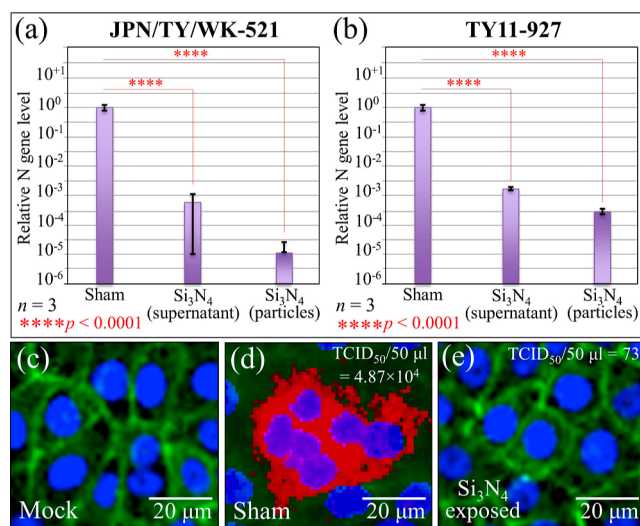
Figure 7. Results of RT-PCR tests to evaluate viral RNA fragmentation using the relative N gene level for (a) JPN/TY/WK-521 and (b) TY11-927 viral strains (a comparison is given using evaluations of supernatants and powders with viral RNA from virions simply suspended in water). Labels in the inset to (a,b) specify statistics according to the unpaired two-tailed Student's test. Fluorescence micrographs of (c) noninoculated cells (mock), (d) cells inoculated with virions unexposed to Si_3N_4 powder (sham), and (e) cells inoculated with TY11-927 supernatant virions exposed for 1 min to a suspension of 5 vol % Si_3N_4 micrometric powder (results of the $TCID_{50}$ assay are given in the inset).

virions and virions on pellets were tested. In comparison with the powder-unexposed control supernatant (sham sample), the viral RNA underwent severe damage after Si_3N_4 contact, and viral RNA was hardly detected on the pelleted powder, this experimental output being common to both variants with high statistical validity. Immunofluorescence images of VeroE6/TMPRSS2 cells are shown in Figure 7c−e in the case of noninoculated cells (mock), cells inoculated with TY11-927 virions unexposed to the Si_3N_4 powder (sham), and
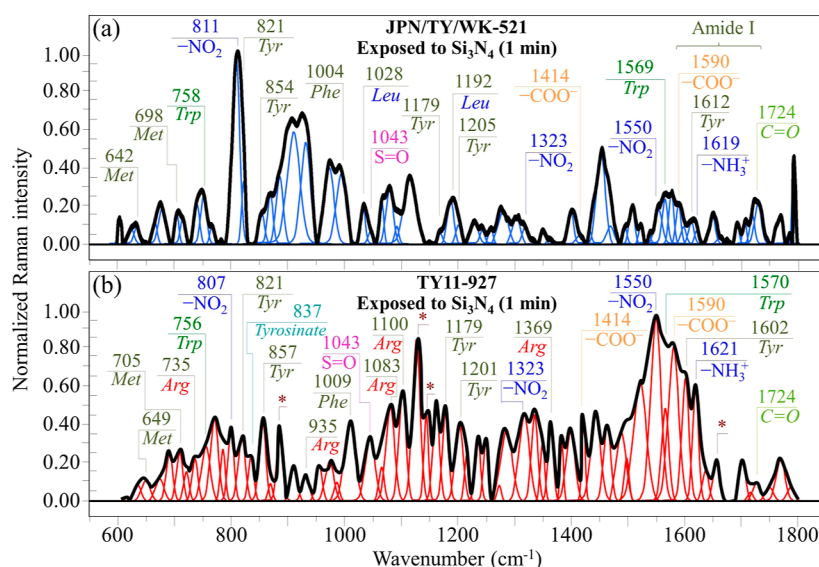
Figure 8. Raman spectra in the wavenumber interval 600−1800 cm^{-1} of (a) JPN/TY/WK-521 and (b) TY11-927 variants after exposure for 1 min to 5 vol % Si$_3$N$_4$ particles in an aqueous suspension; spectra were normalized to their maximum signal and deconvoluted into Lorentzian−Gaussian band components. Four zones are emphasized in (a), and labels show frequencies at the maximum of selected bands (abbreviations are the same as those shown in Figure 1). In (b), asterisks represent bands enhanced by the deimination of the guanidinium group of arginine, while additional specific vibrations related to structural modification upon Si$_3$N$_4$ powder treatment are emphasized and discussed in the text.

cells inoculated with supernatant TY11-927 virions exposed for 1 min to a water solution containing a suspension of 5 vol % Si$_3$N$_4$ powder, respectively. In the images, the antibody of the anti-Coronavirus Spike S1 stained red, thus representing a marker for the synthesis of viral proteins. The viable cell F-actin (phalloidin-stained) displayed green and the cell nuclei (DAPI-stained) displayed blue. The as-cultured cells, un-exposed to virions (mock sample), showed no red staining (cf. Figure 7c), obviously reflecting the absence of virions, while images of the sham cell sample revealed extensive cell infection by the virus (cf. Figure 7d). Remarkably, almost no infected cells were found in the sample inoculated with supernatant virions treated with Si$_3$N$_4$, which appeared indistinguishable from the mock sample (cf. Figure 7e). Data by RT-PCR analyses and fluorescence imaging were confirmed by testing using the TCID$_{50}$ assay (cf. data in the inset to Figure 7d,e). Compared with the negative control (sham sample), the Si$_3$N$_4$ powder produced 99.85% effective inactivation of SARS-CoV-2 TY11-927 virions. This result was similar to that previously reported for the JPN/TY/WK-521 variant with an effective inactivation of 99.28%.[12,13] The combination of the TCID$_{50}$ assay, RT-PCR, and fluorescence spectroscopy results provides unequivocal evidence for the occurrence of SARS-CoV-2 Delta variant inactivation by Si$_3$N$_4$ bioceramic powder. In our previous work on the antipathogenic properties of Si$_3$N$_4$,[12,13,15−19,64] we have suggested that ammonia eluted by hydrolytic reactions taking place at the Si$_3$N$_4$ surface in an aqueous solution plays a fundamental role in the lysis of pathogens and inactivation of viral strains including the JPN/TY/WK-521 variant. In order to substantiate the mechanisms of viral inactivation, we applied Raman spectroscopy to screen the structural details of inactivated virions at the molecular scale.

Zone I—Figure 8 shows the normalized and deconvoluted Raman spectra in the frequency interval 600−1800 cm^{-1} of JPN/TY/WK-521 and TY11-927 variants [in (a and b), respectively] after 1 min exposure to Si$_3$N$_4$ powder suspended

in an aqueous solution. The spectra collected on Si$_3$N$_4$-exposed virions appeared very different to the ones collected on the respective unexposed virions (cf. Figure 1) and to each other as well. The presence of such bold differences proves the ability of Raman spectroscopy to capture peculiar molecular-scale variations of the virion structure, as induced by contact with Si$_3$N$_4$ particles. We performed high spectrally resolved analyses in zones I−IV (i.e., the same zones selected for Figures 2−5) in order to locate the main structural variations inferred by Si$_3$N$_4$ exposure on virions of the two studied variants. These spectral analyses are shown in Figure 9 (zones I and II) and Figure 10 (zones III and IV). Normalized and deconvoluted (average) Raman spectra collected on JPN/TY/WK-521 and TY11-927 variants before and after exposure to Si$_3$N$_4$ powder were screened for spectral differences. Figure 9a,b depicts the Raman spectra collected in spectral zone I (600−750 cm^{-1}) on JPN/TY/WK-521 and TY11-927 variants, respectively. The upper and lower spectra in each section are from virions before and after Si$_3$N$_4$ exposure (cf. labels). Spectral analyses in the low-wavenumber zone I, which is dominated by vibrational signals related to the C−S bond,[33,34,40] enable capturing with high sensitivity the effect of nonradical and free radical structures on methionine and cysteine rotamers.[65,66] The Raman data in Figure 9 show clear wavenumber shifts and significant variations in relative intensity among bands from different rotamers when comparing spectra collected before and after exposure to Si$_3$N$_4$ powder (cf. upper and lower spectra in Figure 9a,b). Structural changes in methionine residues prove that, in both variants, exposure to the Si$_3$N$_4$ surface stressed the virions' structure and induced a change in the population of the rotameric forms of S-containing amino acid residues. However, details of structural alterations differed in the two variants. Important fingerprints of post-translational modifications induced by the interaction of the JPN/TY/WK-521 variant with Si$_3$N$_4$ consisted in a clear reduction in intensity and a shift toward higher wavenumbers (i.e., from 698 to 712 cm^{-1}) of the C−S stretching band of the *gauche*
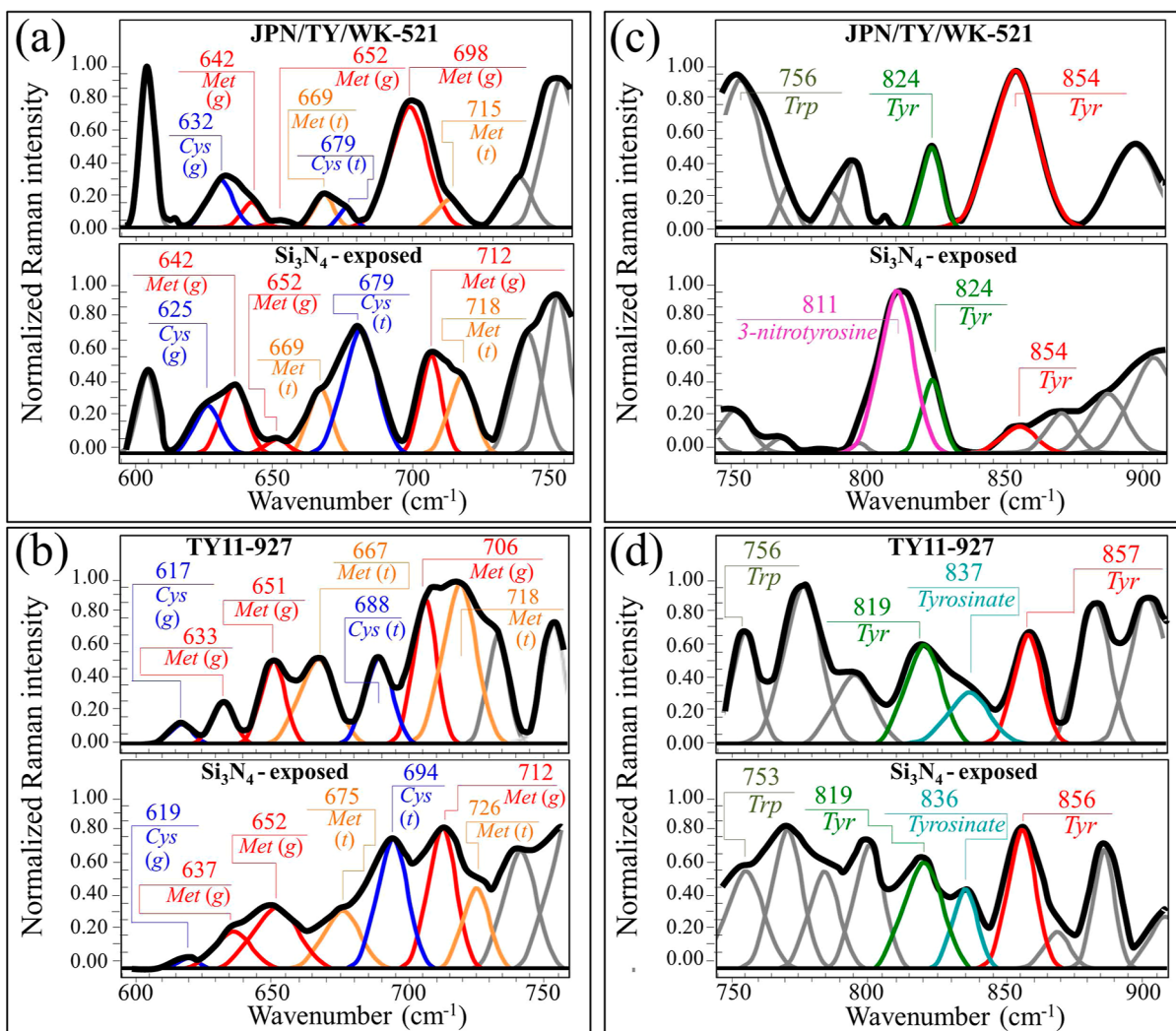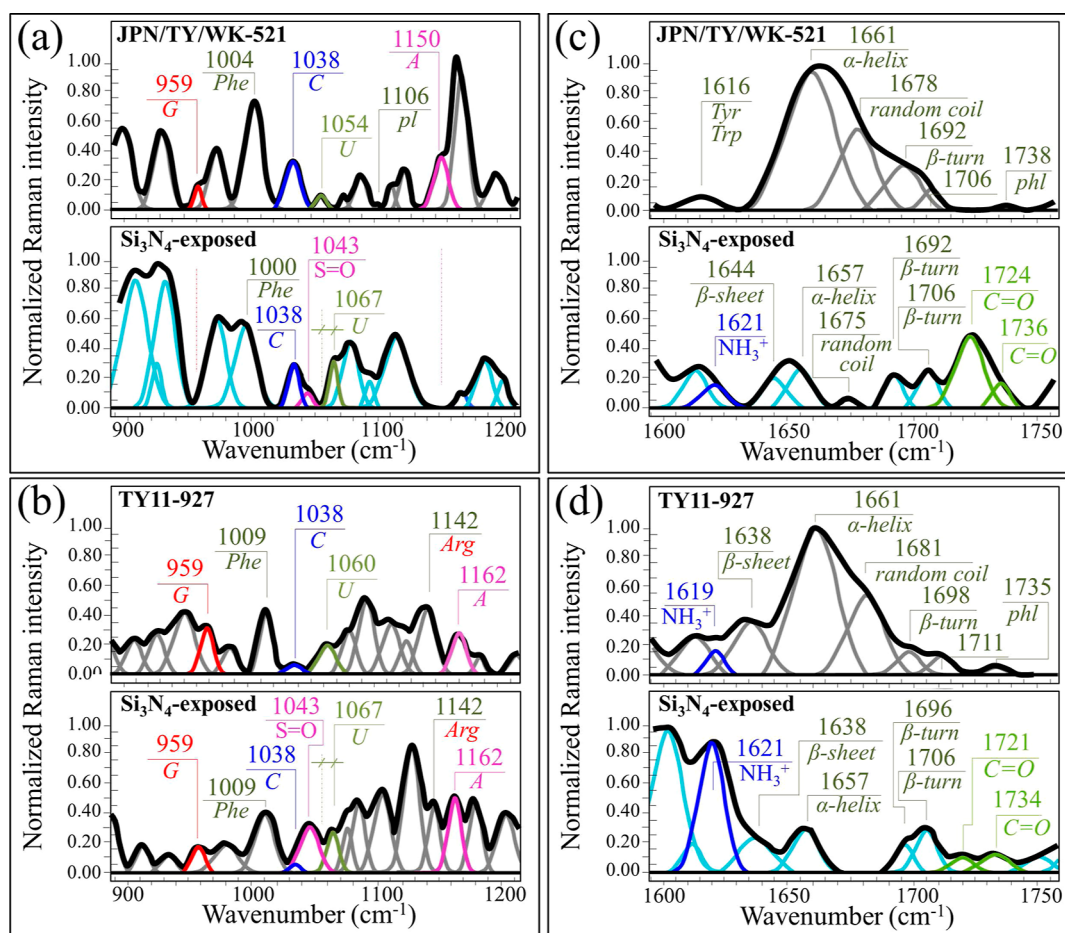
Figure 9. Enlarged Raman spectra in zone I for (a) JPN/TY/WK-521 and (b) TY11-927 strains before and after 1 min exposure to 5 vol % Si_3N_4 micrometric powder in an aqueous suspension (cf. labels in the inset) and in zone II for (c) JPN/TY/WK-521 and (d) TY11-927 variants unexposed and exposed to Si_3N_4 under the same conditions (cf. labels in the inset). Abbreviations are the same as those shown in Figures 2 and 3.

methionine rotamer. According to Torreggiani et al.,[67] these spectral characteristics, together with the appearance of S=O and NH_3^+ signals at 1043 and 1621 cm^{-1}, respectively, reveal the formation of methionine sulfoxide (cf. Figure 8a). These latter two signals, absent in the spectrum of pristine JPN/TY/WK-521 virions, were newly found in the spectrum of virions exposed to Si_3N_4 powder (cf. Figures 1a and 8a). Note that a strong intensification of bands at 1043 and 1621 cm^{-1} was also observed in the spectrum of the TY11-927 virions exposed to Si_3N_4 powder (cf. Figures 1b and 8b). However, significant reduction in intensity and shift toward higher wavenumbers (i.e., from 718 to 726 cm^{-1}) were observed for the C–S stretching band of the *trans* methionine rotamer. Methionine sulfoxide is a post-translational product of methionine, which forms upon oxidation and occurs as a consequence of environmental stress exposure operated by non-radical and free radical species. The interpretation of the observed spectral variations as a consequence of methionine sulfoxide formation is supported by a significant enhancement of two bands from –COO^- terminal bonds, whose symmetric and antisymmetric stretching vibrations are displayed at 1414 and 1590 cm^{-1}, respectively (cf. Figures 1 and 8). In the next section, a discussion is presented about the nonradical or radical

reactions causing methionine oxidation at the surface of Si_3N_4 bioceramics.

Zone II—In Figure 9c,d, Raman spectra are displayed for the spectral region 750−900 cm^{-1}, as collected on JPN/TY/WK-521 and TY11-927 variants, respectively [upper and lower spectra in each section for virions before and after Si_3N_4 exposure (cf. labels)]. The intensity ratio, I_{854}/I_{824}, of the tyrosine doublet, diagnostic of the H-bonding environment around the tyrosine units, was altered by instantaneous contact with Si_3N_4 powder. However, the morphological change of the tyrosine doublet for the TY11-927 variant was less dramatic than that observed for the JPN/TY/WK-521 isolate. In the latter isolate, a trend inversion was recorded upon exposure to Si_3N_4, with the intensity ratio, I_{854}/I_{826}, changing from 1.9 to 0.12. On the other hand, no trend inversion but only a slight increase in the I_{857}/I_{819} ratio (i.e., from 1.1 to 1.2) was observed for the TY11-927 variant. Ammonia induces nitration in the protein tyrosine unit in biological systems,[68] with the formation of 3-nitrotyrosine, while a shift toward higher environmental pH values promotes the formation of tyrosine anions, also referred to as tyrosinate, as achieved by phenol ring hydroxyl deprotonation.[43] Raman spectroscopic studies of these processes[43,68] have revealed that the intensity ratio of the

Figure 10. Enlarged Raman spectra in zone III for (a) JPN/TY/WK-521 and (b) TY11-927 strains before and after 1 min exposure to 5 vol % Si_3N_4 micrometric powder in an aqueous suspension (cf. labels in the inset) and in zone IV for (c) JPN/TY/WK-521 and (d) TY11-927 variants unexposed and exposed to Si_3N_4 under the same conditions (cf. labels in the inset). Abbreviations are the same as those shown in Figures 4 and 5.

phenol ring tyrosine doublet is a useful nitration indicator and proposed clear procedures for spectroscopically recognizing the occurrence of the above molecular modifications of tyrosine. Note that, as discussed later in more detail, both ammonia formation and pH enhancement are the two main environmental perturbations occurring at the Si_3N_4 surface.[15,16] The trend inversion of the tyrosine doublet relative intensity and additional markers of nitration, such as the appearance of signals from the nitro group, $-NO_2$ (i.e., symmetric and asymmetric stretching at ~1323 and ~1550 cm^{-1}, respectively, and in-plane bending vibrations at ~811 cm^{-1}),[69,70] evince the occurrence of severe nitration in Si_3N_4-exposed JPN/TY/WK-521 virions (cf. Figure 9c). As discussed later, nitration of tyrosine residues is also expected to induce bold alterations of the protein secondary structure.[71] Less pronounced morphological changes were seen in the tyrosine doublet of Si_3N_4-exposed TY11-927 virions. However, the slight increase in the I_{857}/I_{819} ratio was consistent with a fractional increase in tyrosinate anions as a consequence of local pH buffering. Following the discussion given in a previous section, the observed mild increase in relative intensity of the 837 cm^{-1} tyrosinate band after exposure to Si_3N_4 is consistent with an increase in environmental pH at the virion/ environment interface.

Zone III—Short-term exposure to Si_3N_4 powder induced bold modifications in the RNA purine and pyrimidine ring vibrations of JPN/TY/WK-521 virions (Figure 10a). Raman markers of RNA purines, namely, C−N−C in plane ring deformation in guanine and the C−N ring stretching mode in adenine (at 959 and 1150 cm^{-1}, respectively) completely disappeared. However, regarding RNA pyrimidines, the spectroscopic marker of uracil base at 1054 cm^{-1} was ~4-fold stronger in relative intensity and shifted by ~13 cm^{-1} toward higher wavenumbers, while the cytosine signal at ~1038 cm^{-1} remained conspicuously unaltered. Regarding TY11-927 virions, a comparison between zone III Raman spectra before and after Si_3N_4 exposure (Figure 10b) revealed an intensity reduction (but not a complete disappearance) of the guanine signal at 959 cm^{-1}, while the 1162 cm^{-1} signal of the other purine, adenine, became stronger (rather than disappearing, as observed in the JPN/TY/WK-521 isolate). On the other hand, only minor alterations could be found for the pyrimidine Raman markers, with the weak band of cytosine at 1038 cm^{-1} remaining unaltered and the uracil band at 1060 cm^{-1} being shifted to 1067 cm^{-1} without significant changes in intensity. Despite differences in structural details between variants, the spectroscopic findings in zone III are in line with the severe fragmentation of viral RNA found by RT-PCR analyses (cf. Figure 7a,b). Following the hypothesis that the post-translational modifications in methionine and tyrosine structures (observed in spectral zones I and II, respectively) could arise from the action of free radicals (as also suggested by the appearance of the S═O band from methionine sulfoxide in Figure 10a,b), it could be hypothesized that
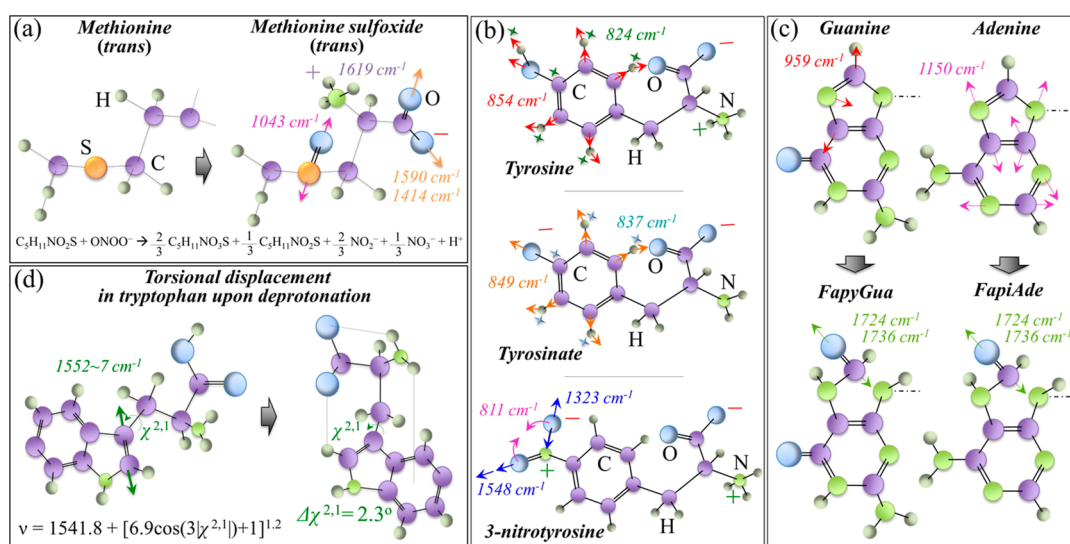
Figure 11. (a) Structures and C−S stretching vibrational modes and wavenumbers of the *trans* methionine rotamer after sulfoxidation of the methionine structure upon a chemical reaction with peroxynitrite, as shown in the inset; (b) structures of tyrosine, tyrosinate, and 3-nitrotyrosine (cf. labels) are shown together with their characteristic vibrational modes and fingerprint wavenumbers. Note the symmetric stretching and in-plane bending modes and the wavenumbers characteristic of the nitro group, −NO$_2$, of the 3-nitrotyrosine structure. (c) Schematic draft of guanine and adenine RNA purines with their respective ring vibrational fingerprints (C−N−C in-plane ring deformation at 959 cm^{-1} and the C−N ring stretching mode at 1150 cm^{-1} for guanine and adenine, respectively). Their transformation into formamidopyrimidines upon opening of the imidazole ring and subsequent oxidation is marked by a new C=O stretching mode appearing at 1724 and 1736 cm^{-1} (cf. Figure 10c,d).

significant oxidation might have occurred on specific RNA bases. Douki and Cadet[72] examined the oxidizing effect of peroxynitrite anions (O=NOO$^-$) on RNA purines and found the formation of 8-oxo-7,8-dihydro-2′-deoxyguanosine (8-oxo-dGuo) at a very low yield linked to the evolution of 2,6-diamino-4-hydroxy-5-formamidopyrimidine (FapyGua). Similar findings could be extended to 4,6-diamino-5-formamido-pyrimidine (FapyAde) as an oxidation product of the adenine base.[73] In support to this hypothesis is the presence of the two C=O stretching signals at 1721−1736 cm^{-1} in zone IV (cf. Figure 10c,d) as a consequence of the formation of Fapy molecules (i.e., C=O bonds in open Fapy rings). As discussed in a previous paper,[13] the invariance of the cytosine signal upon exposure to Si$_3$N$_4$, as found for both variants, is a consequence of 6-hydroxy-5,6-dihydrocytosine (cytosine photohydrate) formation being only possible under high radiative energy.[74] Regarding the shift of the uracil band toward a higher wavenumber, it can be explained as the consequence of an amide−imidic acid tautomeric shift induced by the robust pH buffering at the interface between Si$_3$N$_4$ and virions where local pH reaches values comparable with the uracil ionization pK value.[13,75] The present data are in line with the study by Nonoyama et al.[76] reporting that both cytosine and uracil are almost inert to the peroxynitrite anion (cf. also discussion in the next section). It should be noted that ssRNA viruses are generally prone to the attack of ammonia through the related formation of nitrogen radicals, their genome being quite susceptible to degradation. The complete disappearance of ring vibrations in both guanine and adenine observed in the Si$_3$N$_4$-exposed JPN/TY/WK-521 virions could only be explained by the breakage of the imidazole ring by oxygen/nitrogen radicals to form formamidopyrimidines (Fapy).[77] However, the susceptibility to free radicals might considerably vary among viruses, as observed here for the TY11-927 variant. Viruses with more stable genome types may present slower inactivation kinetics, mainly driven by the degradation of viral proteins.[20]

The Delta variant seems indeed to belong to this latter type of virions as it showed a significantly less amount of RNA damage and slower degradation of viral proteins as compared to the Japanese Kappa isolate. However, despite the lower amount of damage, the level of inactivation recorded by immunochemistry analyses was yet a remarkable entity (cf. Figure 7a,b).

Zone IV—The amide I region is representative of the secondary structure of viral proteins. Comparisons between pristine and Si$_3$N$_4$-exposed virions for this spectral zone are shown in Figure 10c,d for JPN/TY/WK-521 and TY11-927 strains, respectively. Exposure to Si$_3$N$_4$ induced similarly marked variations in the protein secondary structure for both types of virions. Features common to both strains are as follows: a significant fractional decrease in the α-helix structure, complete or almost complete disappearance of the random coil fraction, a relative increase or only a moderate decrease of the β-sheet fraction, and a reshuffling in the balance of β-turn rotamers. Raman spectroscopy is very sensitive to post-translational modifications in proteins and is widely exploited in therapeutic production, in which subtle changes are associated with key structural rearrangements.[78] Fung and Liu[79] have recently reviewed post-translational modifications of Coronavirus proteins, including the spike, envelope, membrane, and nucleocapsid proteins, and emphasized their fundamental impact on viral replication and pathogenesis. Raman spectroscopic assessments cannot provide a direct link between changes in the protein secondary structure and specific proteins responsible for the loss or enhancement of viral infectivity. However, the rotameric variations observed in S-containing amino acid residues are key to interpreting protein structural changes and viral inactivation because disulfide bonds regulate folding, trafficking, and trimerization of the spike protein. The observed rotameric modifications in zone I are indeed connected to unfolding of the α-helical structure after coming in contact with Si$_3$N$_4$. Methionine has an especially high helix-forming

propensity,[80] but sulfoxidation of helical methionines is a strong trigger for destabilization of the native α-fold configuration and leads to a conformational switch into β-sheet and β-turn structures with an increase in structural flexibility.[81] The disappearance of the random coil structure, common to both variants after exposure to Si_3N_4 powder, is another quite interesting feature. Among post-translational folding switches,[82] those involving redox-sensitive cysteine thiols are capable of forming reversible disulfide bonds, by which order ⇔ disorder transitions can be promoted with reversible alterations of the protein function depending on the redox environment.[83,84] There are other examples of intrinsically disordered viral proteins undergoing the disorder-to-order transition under redox or increasingly alkaline environments.[85,86] Leaving aside the intrinsic mechanisms leading to the observed structural changes, which require additional investigations, the present Raman data demonstrate that post-translational modifications involving redox-sensitive cysteine thiols are essential in the observed viral inactivation pathway.

Schematic drafts of the molecular modifications induced upon contact with Si_3N_4 powder are summarized in Figure 11: sulfoxidation of the methionine structure, formation of 3-nitrotyrosine, and formation of formamidopyrimidines in (a−c), respectively. Finally, as a confirmation of the post-translational modifications and deprotonation process occurring upon exposing SARS-CoV-2 virions to Si_3N_4 powder, we monitored the variation of tryptophan signals. Clear signatures of tryptophan in the viral assembly were reported to be bands originating from vibrations of (or within) its indole ring: at ∼756 (indole ring breathing), 1228 (H-rocking in the benzene ring), 1330/1360 (doublet from CH_2 vibrations), and 1552 cm^{-1} (C=C stretching in the pyrrole ring).[45] However, due to overlapping with signals from other amino acid residues, we were only able to resolve the first and the last bands in the above list of five. The last band at 1552 cm^{-1} has been used as a sensor for protein subunit interactions.[87] Given the location of the C=C bond, its vibrational frequency is affected by the torsional angle, $\chi^{2,1}$ (cf. Figure 11d). Systematic Raman analyses of a number of tryptophan derivatives have revealed the actual dependence of the C=C bond stretching wavenumber on the torsional angle, $\chi^{2,1}$.[87] Significant wavenumber shifts from the common value of 1554 cm^{-1} (cf. Figure 1a,b) were recorded after exposure to Si_3N_4 in both the investigated variants (i.e., 1569 and 1570 cm^{-1} for JPN/TY/WK-521 and TY11-927 strains, respectively). According to the equation given in the inset to Figure 11d, the initial torsional angle computed for both variants was small (i.e., $\chi^{2,1} = 2.3°$). However, the significant shift toward higher wavenumbers after exposure to Si_3N_4 is a marker of the increased deprotonation and hydrophobicity of virions upon surface contact. The C=C stretching mode of the tryptophan pyrrole ring senses hydrophobic interactions and represents an additional Raman structural marker of the altered conformation of the virions.

■ DISCUSSION

Arginine Signatures in the Delta Variant as Markers of Infectivity. The effective reproductive number estimated for the Delta variant ($R_t = 6−7$) is approximately double that of the original strain and significantly higher than those of all previously circulating variants of concerns.[88] From an epidemiological viewpoint, the increased transmission rate of the Delta variant was linked to its shorter incubation time,[89] shorter serial interval,[90] and higher viral load.[91] However, the chemical origin of such an increased transmission rate is yet unclear. A reduction in the time needed to receive an infectious dose is triggered by mutations that either allow for more efficient entry of the virus into host cells or result in a higher viral load in infectious people. In this study, the challenge is to understand whether Raman molecular finger-prints for a more efficient entry into host cells (i.e., as a cause of higher infectivity) of the Delta variant could be found in its Raman spectrum. If achieved, such an understanding could enable monitoring (and eventually predicting) viral infectivity, levels of inactivation, or reactivity with neutralizing antibodies for reported variants.

The spike protein of the SARS-CoV-2 virus is a type I fusion protein composed of two subunits responsible for receptor binding and membrane fusion.[92] These highly glycosylated proteins, which have undergone continue mutations, determine the infectivity of the virus and its transmissibility in the host.[93] Amino acid changes in the surface of the spike protein can significantly alter viral functions, as suggested by investigations of the effects of the site-specific glycans on infectivity and immune escape.[94] Early research on coronavirus (i.e., preceding the COVID-19 pandemic) indicated putative asparagine(N)-linked glycosylation sites as post-translational modifications on the viral envelope, supporting protein folding and determining infectivity.[95] In particular, the L452R spike receptor-binding motif substitution observed in the Delta variant confers on it increased infectivity by strengthening the interaction between the spike protein and the host-cell ACE2.[96] This mutation, which replaces leucine by arginine,[6] switches the charge from neutral to strongly positive at a key location in the reception binding subunit of the spike protein. Since the ACE2 receptor charge is negative, the L452R mutation makes the spike protein of the Delta variant extremely efficient in binding. Polar in nature, arginine is the most hydrophilic among natural amino acid residues, with its large side-chain guanidinium ($CH_6N_3^+$) group capable of storing up to six hydrogen bonds (cf. inset to Figure S1b). Due to its pK_a of above 12, the arginine positive charge is hardly altered in biological environments. The compatibility of the extremely hydrophilic arginine residue in an overall hydrophobic environment, which is the case of Delta virions (cf. the discussion on the tyrosine doublet), has been discussed in detail by other authors.[97] The five dipolar N−H protons contained in the guanidinium group are capable of donating hydrogen bonds, while one pair of electrons can accept a hydrogen bond. In terms of the potential for interacting with cell membranes, phospholipids can provide mostly hydrogen bond acceptor groups in the form of both ester bonds and phosphate oxygens. There is thus an enormous attraction for Delta virions toward the cell membrane, with a dramatically increased probability for the virions to hook into the negatively charged ACE2 receptor.

Among the arginine markers in the spectrum of the Delta variant, which were discussed in a previous section (cf. Figures 1b and S1b), the one at 935 cm^{-1} (N−C−N symmetric stretching) can be taken as a vibrational fingerprint unique to the guanidinium group (Table S1), and concurrently, its relative intensity might represent a marker for strain infectivity. Notably, this band tends to disappear upon exposure to Si_3N_4 as a consequence of the chemical environment developed at the solid/virion interface. On the other hand, Si_3N_4 exposure seems not to affect the C−NH_2 antisymmetric bending vibration at 1087 cm^{-1},[23,24] which maintains signal intensity

and only slightly shifts toward lower frequencies (i.e., from 1088 to 1083 cm^{-1}; cf. Figures 1b and 8b). One possible explanation for this spectroscopic observation is the post-translational modification of arginine into citrulline through a deimination process. As schematically drawn in Figure S3a, in the deimination process, one of the terminal nitrogens of the arginine side chain is replaced by a double-bonded oxygen, which removes the positive charge and alters the secondary structure of the protein. This structural conversion should completely eliminate the N−C−N symmetric stretching vibrations of the arginine guanidinium group (i.e., the 935 cm^{-1} band, as indeed we observed in Figure 8b) but preserve the C−N−H$_2$ asymmetric bending mode observed at 1083 cm^{-1} (cf. Figure S3a,b). This is indeed what we have observed in the spectrum of Si$_3$N$_4$-exposed TY11-927 virions (cf. Figure 8b). Note that the disappearance of the twin band at 1043 cm^{-1} also from N−C−N stretching vibrations cannot be confirmed because of its complete overlap with the S═O signal from methionine sulfoxide as a byproduct of methionine oxidation (cf. Figures 8b and S3b in the Supporting Information). Consistent with this structural variation is also a clear increase in relative intensity for bands at 1125 cm^{-1} (mainly C−N stretching), 1149 cm^{-1} (C−N−H$_2$ asymmetric bending), and 1655 cm^{-1} (C−N−H$_2$ symmetric bending)[23] upon exposure to Si$_3$N$_4$ powder (cf. bands labeled with an asterisk in Figures 8b and S3b and listed in Table S2). The salient changes in the structure and Raman spectrum upon deimination of arginine are summarized in Figure S3 and Table S2 of the Supporting Information.

In summary, our Raman study suggests that the guanidinium group of arginine from L452R spike substitution is likely the one primarily responsible for the strengthened electrochemical grip on cells of the Delta variant. Arginine possesses two proton donor groups (OH and NH), six proton acceptor sites (N and O), and six or seven bonds enabling molecular rotations. Accordingly, a number of different tautomers and conformers, including hydrated,[98,99] protonated,[100] and alkali-cationized[101,102] structures, are possible upon stabilization by different intermolecular hydrogen bonds.[98] The present Raman experiments suggest that the 935 cm^{-1} (N−C−N symmetric stretching) Raman fingerprint of the guanidinium group can be taken as a marker for strain infectivity and viral inactivation upon deimination. As explained above in agreement with available Raman studies,[98,102,103] markers of different tautomers or conformers of arginine can also be found at distinct wavenumbers. Therefore, the Raman method unfolded chemical processes behind the enhanced infectivity or inactivation of the Delta variant and other variants undergoing L452R spike mutation.

Chemistry Behind Deimination and Post-translational Modifications. In the previous section, we stated that one important reason for Si$_3$N$_4$ inactivation of TY11-927 virions was the switch of their receptor-binding motif from (strongly) positively charged arginine sites into citrulline ones without a net charge. Our Raman data showed that this mutation increased hydrophobicity in the spike protein and led to folding while affecting its secondary structure and function. However, the chemical route for such inactivation remains to be clarified. We hypothesize that it could reside in the cascade of reactions that follow surface hydrolysis of Si$_3$N$_4$.[15,16] Homolytic cleavage of Si−N bonds concurrently liberates nitrogen anions and unpaired electrons.[104] Formation of ammonium/ammonia moieties induces a substantial pH

buffering in the neighborhood of the surface, while free electrons split the surrounding water molecules to form oxygen radicals, which in turn catalyze NH$_3$ oxidation into hydroxyl-amine and initiate a cascade of off−stoichiometric reactions leading to the formation of reactive nitrogen species (i.e., including NO, NO$_2$, and O═NOO$^-$).[105,106] The formation of O═NOO$^-$ at the Si$_3$N$_4$/pathogen biological interface was proved by stimulated emission depletion microscopy of fungal pathogens in a previous study.[107] The N-vacant sites quickly attract oxygen to form surface silanols, which are deprotonated due to the above-mentioned pH buffering effect and thus possess a negative charge (as experimentally proven by Fourier transform infrared spectroscopy).[108] This study, in line with previous findings,[13] suggests that the final products of Si$_3$N$_4$ surface hydrolysis, namely, nitrogen radicals and deprotonated silanols, are key in SARS-CoV-2 viral inactivation. The silanol moieties induce deimination of positively charged arginine to form uncharged citrulline, as proven by studies of protein citrullination on silica particles in an aqueous environment.[109,110] On the other hand, nitrogen radicals induce oxidation of free and peptide-bound methionine to form sulfoxide with a conformational switch toward β-sheet structures,[111] nitration of tyrosine residues with the formation of nitrotyrosine (altering hydrogen bonding interactions with the polar hydroxyl groups key in determining the level of infectivity), and breakage of the imidazole ring in RNA purines to form Fapy structures. Obviously, structural and genomic differences have an impact on the extent of structural damage that a given variant could sustain before losing its infectivity. However, the present data confirm that Si$_3$N$_4$ inactivation pathways have a broad effectiveness and preserve chemical similarities among different SARS-CoV-2 viral strains. Si$_3$N$_4$ hydrolytic reactions induced a similarly strong degree of viral inactivation also in ssRNA Influenza A virions,[19,112] with similarities in radical driven post-translational alterations of methionine C−S bonds and ring opening with formation of FapyGua.

Significance of the Raman Technology in the COVID-19 Pandemic. This study has shown that the increased transmissibility of the TY11-927 Delta variant as compared to that of the JPN/TY/WK-521 Kappa variant has a chemical origin. The continuous insurgence of new variants in countries with a low percent of vaccinated population calls for new technologies to improve the presently available practices of traceability, tracking, and record keeping of the viral spread. This study on the Delta variant, in line with a recent one on different strains of the Alpha variant,[11] demonstrates that the Raman analysis is capable of unveiling bold differences in signals from different variants. Distinctive of the variants, once implemented into a vibrational library, the Raman method with its unique sensitivity to the molecular structure and symmetry could provide insightful and promptly obtainable information as compared to conventional genomic analyses. We have followed here a barcode approach tailored to transform the information contained in the Raman spectrum into easily readable information and used it to compare Delta, Kappa, and two Alpha sub-variants. The unique molecular-scale information obtained by Raman spectroscopy, once empowered with the Raman barcode, could complement genomic analyses by facilitating real-time data access and exchange as essential steps in tracking variants and in estimating their spread and evolutionary mutation rate.

Besides the importance of a swift spectroscopic identification of different variants and the related possibility of visualizing in real time spatiotemporal viral dynamics (a topic discussed in detail in a previous work),[11] this study shows the potential of Raman spectroscopy in uncovering fundamental aspects of enhanced infectivity and viral inactivation at the molecular scale. The possibility of locating vibrational fingerprints of key mutations and of quantifying the fractional balance between amino acid residues and their rotamers directly links to viral fitness and infectivity. It also reflects the genomic interplay with the cellular environment in which the specific viral strain was developed. From the above considerations, it emerges how Raman spectroscopy could provide an invaluable contribution in rationalizing the chemistry of SARS-CoV-2 structural evolution (as modulated by the interplay between genomic and founder-effect-driven kinetics) and viral inactivation (as induced by contact with antiviral agents, monoclonal antibodies, and drugs).

Finally, as a limitation of this Raman study, it should be noticed that the Raman spectra shown in Figure 1 are indeed representative of different variants, as statistically validated by the Pearson's method. However, the Raman data were collected on virion samples fixed in paraformaldehyde, a procedure that might denature the viral proteins, thus altering the Raman barcodes with respect to that of untreated virions. As all samples are treated with exactly the same fixation procedure, the protein denaturation effect is believed to affect in the same way all compared spectra, which still makes the comparison meaningful. Since it is not possible to bring samples with such a high concentration of virions out of the biosafety level 3 (BLS-3) room, improved experiments could in the future only be performed upon setting the Raman device inside a BSL-3 biocontainment facility (cf. the Methods section for sample preparation procedures).

CONCLUSIONS

This study has shown that the unique sensitivity of Raman spectroscopy to the molecular structure and chirality can readily locate the SARS-CoV-2 Delta variant while also providing key information about mutations in its amino acid residues, protein secondary structures, and nucleic acid components. New chemical information was obtained about the relationship between the observed increase in infectivity and the L452R-related arginine side-chain conformation of the spike protein of the Delta variant, enabling more efficient entry into host cells. There was also sufficient sensitivity to typify distinctive conformational differences in S-containing amino acid residues and in amino acid markers of hydrophobicity such as tyrosine and tryptophan. As a further step in Raman analysis, we monitored viral inactivation upon short-term exposure of Delta virions to a 5 vol % fraction of micrometric Si_3N_4 crystallites in an aqueous solution. Arginine deimination, methionine sulfoxidation, and tyrosine nitration were the main detected post-translational modifications of the viral spike protein. Post-translational modifications of the spike protein almost completely blocked the SARS-CoV-2 virions from infecting the cells, with their clear Raman fingerprints uncovering the antiviral pathway at the molecular scale. Raman assessments of radical driven post-translational alterations represent promising spectroscopic protocols for assessing the effectiveness of future antiviral therapies. In the long-term, Raman identification of the molecular species will allow clear spectral demarcations among different SARS-CoV-2 strains and likely become a key advance in fighting the hardly predictable evolutions of the COVID-19 pandemic scenario.

METHODS

Preparation of SARS-CoV-2 Variants for Raman Analysis. SARS-CoV-2 virus experiments were conducted in a BSL-3 biocontainment facility using BSL-3 work practices. Viral stocks of the original Kappa variant (JPN/TY/WK-521) and Delta variant (TY11-927) were obtained from the Japanese National Institute of Infectious Diseases after detailed genomic characterizations on a series of biological replicates. Viruses were infected at a multiplicity of infection of 0.01 and propagated in the VeroE6/TMPRSS2 cells at 37 °C for 2 days. Each 90 mL sample of the culture supernatants was harvested and centrifuged at 4800 rpm for 20 min. The clarified supernatants were assayed using viral infectivity titers using $TCID_{50}$ (median tissue culture infectious dose method). The titer was in the order of 10^7 $TCID_{50}$/mL for both variants. Supernatants were then concentrated 1/15 using an ultra-filtration membrane, Amicon Ultra-15 centrifugal filter unit (Merck, Darmstadt, Germany). The concentrates were suspended in phosphate-buffered saline (PBS) (−) and ultracentrifuged at 24000 rpm for 3 h at 4 °C. After removing the supernatants, the pellets were resuspended in 50 μL of PBS (−), put on glass-bottom dishes, and air-dried. After fixing the samples with 4% paraformaldehyde for 20 min at room temperature and washing them with distilled water twice, the pellets were air-dried again, kept in a dry environment at 4 °C, and utilized for Raman analyses. The concentration of virus on the glass bottom in Raman measurements was equivalent to 10^9 $TCID_{50}$/38.5 mm^2 for both variants. The area of the glass bottom (7 mm in diameter) was 38.5 mm^2.

Raman Spectroscopy and Related Data Treatments. A Raman spectrometer (LabRAM HR800, HORIBA/Jobin-Yvon, Kyoto, Japan) was used for in situ spectral analysis of viral strains. The spectroscope was set in the confocal mode and equipped using a holographic notch filter to concurrently provide high-efficiency and high-resolution spectral acquisitions. The wavelength of the incoming light was 785 nm, as emitted from a solid-state laser source operating at 10 mW. The background spectrum of paraformaldehyde only was preliminary recorded under the red light using exactly the same spectroscopic measurement conditions. Under red light, the paraformaldehyde used for fixation appeared as a broad background, which could easily be eliminated according to a standardized procedure, as explained later in this section. A spectral resolution better than 1 cm^{-1} was achieved upon analyzing the Raman scattered light using a double monochromator connected with an air-cooled charge-coupled device (CCD) detector (Andor DV420-OE322; 1024 × 256 pixels); the grating used in the spectrometer had the high resolution of 1800 gr/mm. The acquisition time of a single spectrum was typically 10 s. However, several consecutive acquisitions were performed at the same spot to minimize noise. The laser spot was ∼2 μm, as focused on the sample through a 50× optical lens. Construction of average spectra consisted in collecting and averaging 10 spectra at different locations over a total area of ∼2 mm^2 for each type of the sample. A schematic draft explaining the sample setup and the sample/probe interaction is given in the Supporting Information (Figure S4).

Raman spectra were pretreated using a procedure of baseline subtraction due to the presence of a broad fluorescence noise

from paraformaldehyde fixation, as stated above. In order to optimize and standardize the baseline subtraction procedure, three different methods were compared: polynomial fitting,[113] the asymmetric least squares method,[114] and penalized spline smoothing based on vector transformation.[23] In background removal by polynomial fitting,[113] the background is fitted to a low-order polynomial by iteratively determining the polynomial parameters that minimize a least squares criterion. This method is conceptually the simplest and is widely used in Raman spectroscopy. However, besides being time-consuming, it might give unreliable results when baseline drifts arise from fluorescence noise. Due to the presence of a broad and irregular fluorescence spectrum from paraformaldehyde, baseline shifts differed at different locations or even at the same location when different wavenumber intervals were selected. In order to counteract severe baseline drifting, the spectral preprocessing was optimized in order to be insensitive to the noise morphology. For this purpose, the algorithms proposed in refs 114 and 115 were tested, and both proved reliable for the present Raman analyses. The data shown here were processed according to the penalized spline smoothing algorithm based on vector transformation, as given in ref 115. An example of background subtraction is shown in Figure S5 of the Supporting Information.

After baseline subtraction, Raman spectra were automatically deconvoluted into a series of Gaussian−Lorentzian sub-bands using commercial software (LabSpec 4.02, HORIBA/Jobin-Yvon, Kyoto, Japan). In deconvolutive spectral analyses, we applied a machine learning approach using an automatic solver built in-house, $S_{av}(\nu)$, exploiting a linear polynomial expression of Gaussian−Lorentzian functions, $V(\Delta\nu, \sigma, \gamma)$, where ν, $\Delta\nu$, σ, and γ represent the Raman frequency, the shift in frequency from each sub-band's maximum (ν_0), the standard deviation of each Gaussian−Lorentzian component, and the full-width at half-maximum of the Lorentzian component, respectively. An algorithm searching for the minimum value of the difference between the experimental spectrum and the fitted spectrum was then set as follows

$$ S_{av}(\nu) - \sum_i \alpha_i \sum_j \beta_{ij} V_{ij}(\nu_0, \ \Delta\nu, \ \sigma, \ \gamma) \cong 0 \tag{1} $$

where the index i locates each compound in a series of n compounds contributing to the overall spectrum and the index j locates each Gaussian−Lorentzian sub-band of a series of m compounds in the Raman spectrum of each compound of an n series. A computer program was utilized to optimize the above algorithm after choosing a series of Gaussian−Lorentzian sub-bands from the deconvoluted spectra of preselected compounds included in a database of key biomolecules and compounds in aqueous solution and in the solid state according to the chemical and structural peculiarities of virions. Preselection of the compounds was performed according to the published Raman literature on viruses.[44,45,47] After picking up the spectral sub-bands of selected elementary compounds from the library, the algorithm pinpointed the closest matches to the experimental spectra according to the three following criteria: (i) assigning spectral positions (ν_0) of sub-bands from each selected elementary compound within ±3 cm^{-1} (i.e., to include the possibility of alterations of the molecular structure in the virion structure); (ii) preserving relative intensities (β_{ij}) upon summing up the selected sub-bands; and (iii) preserving the full-width at half-maximum (σ and γ) values for specific sub-bands from each elementary

compound. The conditions imposed on band positions, relative intensities, and bandwidths provided a set of mathematical constraints that allowed univocally deconvoluting the experimental spectra. The computational work produced two important outcomes: (a) spectra could be screened automatically and an appropriate deconvolution could be suggested through finding the closest match with the experimentally collected spectrum through eq 1, while additionally identifying the molecules/compounds primarily contributing to each sub-band, and (b) sub-bands having primarily single-reference-molecule sourced signal intensity (>90%) could be isolated. A number of reference spectra from basic molecules used in the above-described machine learning algorithm could be found in ref 112.

Statistical Analyses. Pearson's correlation coefficient (PC), r, also referred to as the spectral similarity coefficient, was calculated according to the following equation[21]

$$ r = \frac{\sum_{i=1}^{n} \Theta_i s_i - (\sum_{i=1}^{n} \Theta_i \sum_{i=1}^{n} s_i)}{\sqrt{\left[\sum_{i=1}^{n} \Theta_i^2 - \frac{1}{n}(\sum_{i=1}^{n} \Theta_i)^2\right]\left[\sum_{i=1}^{n} s_i^2 - \frac{1}{n}(\sum_{i=1}^{n} s_i)^2\right]}} \tag{2} $$

where Θ represents the average spectrum from a given variant, s is the individual spectrum to be statistically evaluated, and n is the total number of CCD pixels in each of the two spectra. Note that the wavenumber interval object of the comparison and the individual pixel intervals selected should be exactly the same. A perfect matching and a complete mismatch between Θ and s then give $r = 1$ and $r = 0$, respectively.

Statistical analyses of the RT-PCR results were carried out by means of the unpaired Student's t-test. The statistical significance of the data was evaluated as highly statistically relevant ($p < 0.01$; labeled with two or more asterisks).

Assessment of Virus Infectivity and Immunochemistry Assays. A fraction of 5 vol % Si_3N_4 powder was dispersed in 1 mL of PBS (−), followed by the addition of viral suspensions of each variant [2 × 10^5 median tissue culture infectious dose (TCID$_{50}$) in 20 μL]. The Si_3N_4 powder (SINTX Technologies, Inc., Salt Lake City, UT, USA) had a particle size of 0.8−1.0 μm. Mixing was gently performed at room temperature for 1 min by slow manual rotation. After exposure to virions, the powders were pelleted by centrifugation (2400 rpm for 2 min), followed by filtration through a 0.22 μm filter (Hawach sterile PES syringe filter, Hawach Scientific Co., Ltd., Xi'an, China). Supernatants and pellets were collected, aliquoted, and then subjected to RT-PCR tests using N gene primers. The RNA of viruses exposed or unexposed to Si_3N_4 particles was extracted using a QI Amp Viral RNA mini kit (QIAGEN N.V., Hilden, Germany) according to the manufacturer protocol. Reverse transcription was performed using a ReverTra Ace qPCR RT master mix (TOYOBO CO., LTD., Osaka, Japan). 8 μL of the RNA template was added to 2 μL of the 5× RT master mix. The mixture was incubated at 37 °C for 15 min, 50 °C for 5 min, and 98 °C for 5 min, and held at 4 °C.

Supernatant virions exposed or unexposed to Si_3N_4 powder were inoculated into VeroE6/TMPRSS2 cells grown in growth medium and maintained at 37 °C in an atmosphere of 5% CO$_2$. The infectivity titer was in all cases in the order of 10^7 TCID$_{50}$/mL. After infection at a multiplicity of infection of 0.01 at 37 °C for 2 days, the infected cells were washed with Tris-buffered saline (TBS) buffer (20 mM Tris-HCl, pH 7.5, 150 mM NaCl) and fixed with 4% perfluoroalkoxy alkane for

10 min at room temperature, followed by membrane permeabilization with 0.1% Triton X in TBS for 15 min at room temperature. The cells were blocked with 2% fetal bovine serum in PBS (−) for 60 min at room temperature and stained with the anti-SARS Coronavirus Spike S1 (Rabbit) antibody (dilution = 1:60) (Sino Biological Inc., Beijing, China) for 60 min at room temperature. After washing with wash buffer, cells were incubated with Hoechst 33342 (Dojindo Laboratories, Kumamoto, Japan), Alexa 594 goat anti-rabbit IgG (H + L) (1:500) (Thermo Fisher Scientific, Waltham, MA, USA), and Alexa 488 phalloidin (1:40) (Thermo Fisher Scientific, Waltham, MA, USA) for 60 min at room temperature in the dark. Infected cells were visualized using the Keyence BZ-X analyzer. The inoculated VeroE6/TMPRSS2 cells were stained red, green, and blue to visualize the viral protein, F-actin, and cell nuclei, respectively.

■ ASSOCIATED CONTENT

ⓈⒾ Supporting Information

The Supporting Information is available free of charge at https://pubs.acs.org/doi/10.1021/acsinfecdis.2c00200.

  Methods and additional results (PDF)

■ AUTHOR INFORMATION

Corresponding Authors

Giuseppe Pezzotti − *Ceramic Physics Laboratory, Kyoto Institute of Technology, Kyoto 606-8585, Japan; Department of Immunology, Graduate School of Medical Science, Kyoto Prefectural University of Medicine, Kyoto 602-8566, Japan; Department of Orthopedic Surgery, Tokyo Medical University, 160-0023 Tokyo, Japan; Center for Advanced Medical Engineering and Informatics, Osaka University, Osaka 565-0854, Japan; Institute of Biomaterials and Bioengineering, Tokyo Medical and Dental University, Tokyo 101-0062, Japan; Department of Dental Medicine, Graduate School of Medical Science, Kyoto Prefectural University of Medicine, Kyoto 602-8566, Japan; Biomedical Research Center, Kyoto Institute of Technology, Kyoto 606-8585, Japan;* Ⓞ orcid.org/0000-0002-9663-2429; Email: pezzotti@kit.ac.jp

Osam Mazda − *Department of Immunology, Graduate School of Medical Science, Kyoto Prefectural University of Medicine, Kyoto 602-8566, Japan;* Email: omazda@gmail.com

Authors

Eriko Ohgitani − *Department of Immunology, Graduate School of Medical Science, Kyoto Prefectural University of Medicine, Kyoto 602-8566, Japan*

Yuki Fujita − *Ceramic Physics Laboratory, Kyoto Institute of Technology, Kyoto 606-8585, Japan*

Hayata Imamura − *Ceramic Physics Laboratory, Kyoto Institute of Technology, Kyoto 606-8585, Japan*

Masaharu Shin-Ya − *Department of Immunology, Graduate School of Medical Science, Kyoto Prefectural University of Medicine, Kyoto 602-8566, Japan*

Tetsuya Adachi − *Department of Dental Medicine, Graduate School of Medical Science, Kyoto Prefectural University of Medicine, Kyoto 602-8566, Japan*

Toshiro Yamamoto − *Department of Dental Medicine, Graduate School of Medical Science, Kyoto Prefectural University of Medicine, Kyoto 602-8566, Japan*

Narisato Kanamura − *Department of Dental Medicine, Graduate School of Medical Science, Kyoto Prefectural University of Medicine, Kyoto 602-8566, Japan*

Elia Marin − *Ceramic Physics Laboratory, Kyoto Institute of Technology, Kyoto 606-8585, Japan; Department of Dental Medicine, Graduate School of Medical Science, Kyoto Prefectural University of Medicine, Kyoto 602-8566, Japan;* Ⓞ orcid.org/0000-0002-0981-7821

Wenliang Zhu − *Ceramic Physics Laboratory, Kyoto Institute of Technology, Kyoto 606-8585, Japan;* Ⓞ orcid.org/0000-0001-7532-9714

Ichiro Nishimura − *Division of Advanced Prosthodontics, The Jane and Jerry Weintraub Center for Reconstructive Biotechnology, UCLA School of Dentistry, Los Angeles, California 90095, United States*

Complete contact information is available at:
https://pubs.acs.org/10.1021/acsinfecdis.2c00200

Notes

The authors declare no competing financial interest.

■ ACKNOWLEDGMENTS

■ REFERENCES

(1) Report of the 49th meeting of the COVID-19 advisory board of Ministry of Health, Labour and Welfare of Japan (August 25, 2021). https://www.niid.go.jp/niid/en/2019-ncov-e/10624-covid19-ab49th-en.html, last (accessed June, 11 2022).

(2) Rashed, E. A.; Hirata, A. Infectivity upsurge by COVID-19 viral variants in Japan: evidence from deep learning modeling. *Int. J. Environ. Res. Publ. Health* **2021**, *18*, 7799.

(3) Shiehzadegan, S.; Alaghemand, N.; Fox, M.; Venketaraman, V. Analysis of the Delta variant B.1.617.2 COVID-19. *Clin. Pract.* **2021**, *11*, 778−784.

(4) Planas, D.; Veyer, D.; Baidaliuk, A.; Staropoli, I.; Guivel-Benhassine, F.; Rajah, M. M.; Planchais, C.; Porrot, F.; Robillard, N.; Puech, J.; Prot, M.; Gallais, F.; Gantner, P.; Velay, A.; Le Guen, J.; Kassis-Chikhani, N.; Edriss, D.; Belec, L.; Seve, A.; Courtellemont, L.; Péré, H.; Hocqueloux, L.; Fafi-Kremer, S.; Prazuck, T.; Mouquet, H.; Bruel, T.; Simon-Lorière, E.; Rey, F. A.; Schwartz, O. Reduced sensitivity of SARS-CoV-2 variant Delta to antibody neutralization. *Nature* **2021**, *596*, 276−280.

(5) Callaway, E. The mutation that helps Delta spread like wildfire. *Nature* **2021**, *596*, 472−473.

(6) Pecho-Silva, S.; Barboza, J. J.; Navarro-Solsol, A. C.; Rodriguez-Morales, A. J.; Bonilla-Aldana, D. K.; Panduro-Correa, V. SARS-CoV-2 Mutations and Variants: what do we know so far? *Microbes Infect. Chemother.* **2021**, *1*, No. e1256.

(7) Srivastava, S.; Garg, I.; Bansal, A.; Kumar, B. SARS-CoV-2 infection: physiological and environmental gift factors at high altitude. *VirusDisease* **2020**, *31*, 450−452.

(8) Afrin, S. Z.; Paul, S. K.; Begum, J. A.; Nasreen, S. A.; Ahmed, S.; Ahmad, F. U.; Aziz, M. A.; Parvin, R.; Aung, M. S.; Kobayashi, N. Extensive genetic diversity with novel mutations in spike glycoprotein of severe acute respiratory syndrome coronavirus 2, Bangladesh in late 2020. *New Microbes New Infect.* **2021**, *41*, 100889.

(9) Liu, Y.; Liu, J.; Johnson, B. A.; Xia, H.; Ku, Z.; Schindewolf, C.; Widen, S. G.; An, Z.; Weaver, S. C.; Menachery, V. D.; Xie, X.; Shi, P.-Y. Delta spike P681R mutation enhances SARS-CoV-2 fitness over Alpha variant. *Cell Rep.* **2022**, *39*, 110829.

(10) Bale, R.; Iida, A.; Yamakawa, M.; Li, C. G.; Tsubokura, M. Quantifying the COVID 19 infection risk due to droplet/aerosol inhalation, **2021**. arxiv.org/abs/2110.04295

(11) Pezzotti, G.; Boschetto, F.; Ohgitani, E.; Fujita, Y.; Shin-Ya, M.; Adachi, T.; Yamamoto, T.; Kanamura, N.; Marin, E.; Zhu, W.; Nishimura, I.; Mazda, O. Raman molecular fingerprints of SARS-CoV-2 British variant and the concept of Raman barcode. *Adv. Sci.* **2021**, *9*, 2103287.

(12) Pezzotti, G.; Ohgitani, E.; Shin-Ya, M.; Adachi, T.; Marin, E.; Boschetto, F.; Zhu, W.; Mazda, O. Instantaneous "catch-and-kill" inactivation of SARS-CoV-2 by nitride ceramics. *Clin. Transl. Med.* **2020**, *10*, No. e212.

(13) Pezzotti, G.; Boschetto, F.; Ohgitani, E.; Fujita, Y.; Shin-Ya, M.; Adachi, T.; Yamamoto, T.; Kanamura, N.; Marin, E.; Zhu, W.; Nishimura, I.; Mazda, O. Mechanisms of instantaneous inactivation of SARS-CoV-2 by silicon nitride bioceramic. *Mater. Today Bio* **2021**, *12*, 100144.

(14) Sengul, A. B.; Asmatulu, E. Toxicity of metal and metal oxide nanoparticles: a review. *Environ. Chem. Lett.* **2020**, *18*, 1659−1683.

(15) Pezzotti, G. Silicon nitride: a bioceramic with a gift. *ACS Appl. Mater. Interfaces* **2019**, *11*, 26619−26636.

(16) Pezzotti, G. A spontaneous solid-state NO donor to fight antibiotic resistant bacteria. *Mater. Today Chem.* **2018**, *9*, 80−90.

(17) Pezzotti, G.; Bock, R. M.; McEntire, B. J.; Adachi, T.; Marin, E.; Boschetto, F.; Zhu, W.; Mazda, O.; Bal, S. B. In vitro antibacterial activity of oxide and non-oxide bioceramics for arthroplastic devices: I. In situ time-lapse Raman spectroscopy. *Analyst* **2018**, *143*, 3708−3721.

(18) Pezzotti, G.; Fujita, Y.; Boschetto, F.; Zhu, W.; Marin, E.; Vandelle, E.; McEntire, B. J.; Bal, S. B.; Giarola, M.; Makimura, K.; Polverari, A. Activity and mechanism of action of the bioceramic silicon nitride as an environmentally friendly alternative for the control of the grapevine downy mildew pathogen Plasmopara viticola. *Front. Microbiol.* **2020**, *11*, 610211.

(19) Pezzotti, G.; Boschetto, F.; Ohgitani, E.; Fujita, Y.; Zhu, W.; Marin, E.; McEntire, B. J.; Bal, B. S.; Mazda, O. Silicon nitride: a potent solid-state bioceramic inactivator of ssRNA viruses. *Sci. Rep.* **2021**, *11*, 2977.

(20) Decrey, L.; Kazama, S.; Kohn, T. Ammonia as an in situ sanitizer: influence of virus genome type on inactivation. *Appl. Environ. Microbiol.* **2016**, *82*, 4909−4920.

(21) Samuel, A. Z.; Mukojima, R.; Horii, S.; Ando, M.; Egashira, S.; Nakashima, T.; Iwatsuki, M.; Takeyama, H. On selecting a suitable spectral matching method for automated analytical applications of Raman spectroscopy. *ACS Omega* **2021**, *6*, 2060−2065.

(22) Zhu, G.; Zhu, X.; Fan, Q.; Wan, X. Raman spectra of amino acids and their aqueous solutions. *Spectrochim. Acta, Part A* **2011**, *78*, 1187−1195.

(23) Hernández, B.; Pflüger, F.; Derbel, N.; De Coninck, J.; Ghomi, M. Vibrational analysis of amino acids and short peptides in hydrated media. VI. Amino acids positively charged side chains: L-lysine and L-arginine. *J. Phys. Chem. B* **2010**, *114*, 1077−1088.

(24) Kumar, S.; Rai, S. B. Spectroscopic studies of L-arginine molecule. *Indian J. Pure Appl. Phys.* **2010**, *48*, 251−255.

(25) Hernández, B.; Pflüger, F.; Nsangou, M.; Ghomi, M. Raman spectra of L-leucine crystals. *J. Phys. Chem. B* **2009**, *113*, 3169−3178.

(26) Kumar, S. Spectroscopic studies of valine and leucine molecules as comparative study. *Elixir Vib. Spec.* **2011**, *39*, 4996−4999.

(27) Sato, E. T.; Martinho, H. First principles calculations of Raman vibrational modes in the fingerprint region for connective tissue. *Biomed. Opt Express* **2018**, *9*, 1728.

(28) Culka, A.; Jehlička, J.; Edwards, H. G. M. Acquisition of Raman spectra of amino acids using portable instruments: outdoor measurements and comparison. *Spectrochim. Acta, Part A* **2010**, *77*, 978−983.

(29) Dhamelincourt, P.; Ramirez, F. J. Polarized micro-Raman and FT-IR spectra of L-glutamine. *Appl. Spectrosc.* **1993**, *47*, 446−451.

(30) Golichenko, B. O.; Naseka, V. M.; Strelchuk, V. V.; Kolomys, O. F. Raman study of L-asparagine and L-glutamine molecules adsorbed on aluminum films in a wide frequency range. *Semicond. Phys. Quantum Electron. Optoelectron.* **2017**, *20*, 297−304.

(31) Navarrete, J. T. L.; Hernández, V.; Ramírez, F. J. Vibrational study of aspartic acid and glutamic acid dipeptides. *J. Mol. Struct.* **1995**, *348*, 249−252.

(32) Harvey, W. T.; Carabelli, A. M.; Jackson, B.; Gupta, R. K.; Thomson, E. C.; Harrison, E. M.; Ludden, C.; Reeve, R.; Rambaut, A.; Peacock, S. J.; Robertson, D. L. COVID-19 Genomics UK (COG-UK) Consortium, Peacock, S. J., and Robertson, D. L. (2021) SARS-CoV-2 variants, spike mutations and immune escape. *Nat. Rev. Microbiol.* **2021**, *19*, 409−424.

(33) Podstawka, E.; Ozaki, Y.; Proniewicz, L. M. Part II: Surface-enhanced Raman spectroscopy investigation of methionine containing heterodipeptides adsorbed on colloidal silver. *Appl. Spectrosc.* **2004**, *58*, 581−590.

(34) Cao, X.; Fischer, G. Conformational and infrared spectral studies of L-methionine and its N-deuterated isotopomer as isolated zwitterions. *J. Phys. Chem. A* **2002**, *106*, 41−50.

(35) Švančarová, P.; Betáková, T. Conserved methionine 165 of matrix protein contributes to the nuclear import and is essential for influenza A virus replication. *Virol. J.* **2018**, *15*, 187.

(36) Ye, Z.; Liu, T.; Offringa, D. P.; McInnis, J.; Levandowski, R. A. Association of influenza virus matrix protein with ribonucleoproteins. *J. Virol.* **1999**, *73*, 7467−7473.

(37) Diaz Fleming, G.; Finnerty, J. J.; Campos-Vallette, M.; Célis, F.; Aliaga, A. E.; Fredes, C.; Koch, R. Experimental and theoretical Raman and surface-enhanced Raman scattering study of cysteine. *J. Raman Spectrosc.* **2009**, *40*, 632−638.

(38) Parker, S. F. Assignment of the vibrational spectrum of L-cysteine. *Chem. Phys.* **2013**, *424*, 75−79.

(39) Bazylewski, P.; Divigalpitiya, R.; Fanchini, G. In situ Raman spectroscopy distinguishes between reversible and irreversible thiol modifications in L-cysteine. *RSC Adv.* **2017**, *7*, 2964−2970.

(40) Hernández, B.; Pflüger, F.; Adenier, A.; Kruglik, S. G.; Ghomi, M. Side chain flexibility and protonation states of sulfur atom containing amino acids. *Phys. Chem. Chem. Phys.* **2011**, *13*, 17284−17294.

(41) Hildebrandt, P. G.; Copeland, R. A.; Spiro, T. G.; Otlewski, J.; Laskowski, M., Jr.; Prendergast, F. G. Tyrosine hydrogen-bonding and environmental effects in proteins probed by ultraviolet resonance Raman spectroscopy. *Biochem* **1988**, *27*, 5426−5433.

(42) Krafft, C.; Hinrichs, W.; Orth, P.; Saenger, W.; Welfle, H. Interaction of Tet repressor with operator DNA and with tetracycline studied by infrared and Raman spectroscopy. *Biophys. J.* **1998**, *74*, 63−71.

(43) Hernández, B.; Coïc, Y.-M.; Pflüger, F.; Kruglik, S. G.; Ghomi, M. All characteristic Raman markers of tyrosine and tyrosinate originate from phenol ring fundamental vibrations. *J. Raman Spectrosc.* **2016**, *47*, 210−220.

(44) Arp, Z.; Autrey, D.; Laane, J.; Overman, S. A.; Thomas, G. J., Jr. Tyrosine Raman signatures of the filamentous virus Ff are diagnostic of non-hydrogen-bonded phenoxyls: demonstration by Raman and infrared spectroscopy of p-cresol vapor. *Biochem* **2001**, *40*, 2522−2529.

(45) Thomas, G. J., Jr. New structural insights from Raman spectroscopy of proteins and their assemblies. *Biopolymers* **2002**, *67*, 214−225.

(46) Siamwiza, M. N.; Lord, R. C.; Chen, M. C.; Takamatsu, T.; Harada, I.; Matsuura, H.; Shimanouchi, T. Interpretation of the doublet at 850 and 830 cm⁻¹ in the Raman spectra of tyrosyl residue in proteins and certain model compounds. *Biochem* **1975**, *14*, 4870−4876.

(47) Overman, S. A.; Aubrey, K. L.; Vispo, N. S.; Cesareni, G.; Thomas, G. J., Jr. Novel tyrosine markers in Raman spectra of wild-type and mutant (Y21M and Y24M) Ff virions indicate unusual

environments for coat protein phenoxyls. *Biochem* **1994**, *33*, 1037−1042.

(48) Deval, H.; Nyayanit, D. A.; Mishra, S. K.; Yadav, P. D.; Zaman, K.; Shankar, P.; Misra, B. R.; Behera, S. P.; Kumar, N.; Kumar, A.; Bhardwaj, P.; Dwivedi, G. R.; Singh, R.; Shete, A. M.; Pandit, P.; Pandey, A. K.; Yadav, G. K.; Gupta, S.; Kumar, M.; Kavathekar, A.; Singh, R. S.; Prajapati, S.; Kant, R. Genome sequencing reveals a mixed picture of SARS-CoV-2 variant of concern circulation in Eastern Uttar Pradesh, India. *Front. Med.* **2022**, *8*, 781287.

(49) Śanchez-Cortés, S.; Garcia-Ramos, J. V. SERS of cytosine and its methylated derivatives on metal colloids. *J. Raman Spectrosc.* **1992**, *23*, 61−66.

(50) Mathlouthi, M.; Seuvre, A. M.; Koenig, J. L. F.T.-I.R. and laser-raman spectra of cytosine and cytidine. *Carbohydr. Res.* **1986**, *146*, 1−13.

(51) Madzharova, F.; Heiner, Z.; Gühlke, M.; Kneipp, J. Surface-enhanced hyper-Raman spectra of adenine, guanine, cytosine, thymine, and uracil. *J. Phys. Chem. C* **2016**, *120*, 15415−15423.

(52) Lopes, R. P.; Marques, M. P. M.; Valero, R.; Tomkinson, J.; de Carvalho, L. A. E. B. Guanine: a combined study using vibrational spectroscopy and theoretical methods. *Int. J. Spectrosc.* **2012**, *27*, 273−292.

(53) Lopes, R. P.; Valero, R.; Tomkinson, J.; Marques, M. P. M.; Batista de Carvalho, L. A. E. Applying vibrational spectroscopy to the study of nucleobases − adenine as a case study. *New J. Chem.* **2013**, *37*, 2691−2699.

(54) Voicescu, M.; Ionescu, S.; Nistor, C. L. Spectroscopic study of 3-hydroxyflavone-protein interaction in lipidic bi-layers immobilized on silver nanoparticles. *Spectrochim. Acta, Part A* **2017**, *170*, 1−8.

(55) Thomas, G. J., Jr.; Hartman, K. A. Raman studies of nucleic acids. 8. Estimation of RNA secondary structure from Raman scattering by phosphate-group vibrations. *Biochim. Biophys. Acta* **1973**, *312*, 311−322.

(56) Maiti, N. C.; Apetri, M. M.; Zagorski, M. G.; Carey, P. R.; Anderson, V. E. Raman spectroscopic characterization of secondary structure in natively unfolded proteins: α-synuclein. *J. Am. Chem. Soc.* **2004**, *126*, 2399−2408.

(57) Eker, F.; Cao, X.; Nafie, L.; Huang, Q.; Schweitzer-Stenner, R. The structure of alanine based tripeptides in water and dimethyl sulfoxide probed by vibrational spectroscopy. *J. Phys. Chem. B* **2003**, *107*, 358−365.

(58) Wang, Y.; Liu, C.; Zhang, C.; Wang, Y.; Hong, Q.; Xu, S.; Li, Z.; Yang, Y.; Huang, Z.; Cong, Y. Structural basis for SARS-CoV-2 Delta variant recognition of ACE2 receptor and broadly neutralizing antibodies. *Nat. Commun.* **2022**, *13*, 871.

(59) Yurkovetskiy, L.; Wang, X.; Pascal, K. E.; Tomkins-Tinch, C.; Nyalile, T. P.; Wang, Y.; Baum, A.; Diehl, W. E.; Dauphin, A.; Carbone, C.; Veinotte, K.; Egri, S. B.; Schaffner, S. F.; Lemieux, J. E.; Munro, J. B.; Rafique, A.; Barve, A.; Sabeti, P. C.; Kyratsous, C. A.; Dudkina, N. V.; Shen, K.; Luban, J. Structural and functional analysis of the D614G SARS-CoV-2 spike protein variant. *Cell* **2020**, *183*, 739−751.

(60) Calcagnile, M.; Forgez, P.; Alifano, M.; Alifano, P. The lethal triad: SARS-COV-2 spike, ACE2 and TMPRSS2. Mutations in host and pathogen may affect the course pandemic, **2021**. bioRxiv: 2021.01.12.426365.

(61) Cherian, S.; Potdar, V.; Jadhav, S.; Yadav, P.; Gupta, N.; Das, M.; Rakshit, P.; Singh, S.; Abraham, P.; Panda, S.; Team, N.; NIC Team. SARS-CoV-2 spike mutations, L452R, T478K, E484Q and P681R, in the second wave of COVID-19 in Maharashtra, India. *Microorganisms* **2021**, *9*, 1542.

(62) Teruel, N.; Mailhot, O.; Najmanovich, R. J. Modelling conformational state dynamics and its role on infection for SARS-CoV-2 Spike protein variants. *PLoS Comput. Biol.* **2021**, *17*, No. e1009286.

(63) Zhao, Z.; Sokhansanj, B. A.; Malhotra, C.; Zheng, K.; Rosen, G. L. Genetic grouping of SARS-CoV-2 coronavirus sequences using informative sub-type markers for pandemic spread visualization. *PLoS Comput. Biol.* **2020**, *16*, No. e1008269.

(64) Pezzotti, G.; Bock, R. M.; McEntire, B. J.; Jones, E.; Boffelli, M.; Zhu, W.; Baggio, G.; Boschetto, F.; Puppulin, L.; Adachi, T.; Yamamoto, T.; Kanamura, N.; Marunaka, Y.; Bal, B. S. Silicon nitride bioceramics induce chemically driven lysis in Porphyromonas gingivalis. *Langmuir* **2016**, *32*, 3024−3035.

(65) Davies, M. J. The oxidative environment and protein damage. *Biochim. Biophys. Acta, Proteins Proteomics* **2005**, *1703*, 93−109.

(66) Schöneich, C. Methionine oxidation by reactive oxygen species: reaction mechanisms and relevance to Alzheimer's disease. *Biochim. Biophys. Acta, Proteins Proteomics* **2005**, *1703*, 111−119.

(67) Torreggiani, A.; Barata-Vallejo, S.; Chatgilialoglu, C. Combined Raman and IR spectroscopic study on the radical-based modifications of methionine. *Anal. Bioanal. Chem.* **2011**, *401*, 1231−1239.

(68) Niederhafner, P.; Šafařík, M.; Neburková, J.; Keiderling, T. A.; Bouř, P.; Šebestík, J. Monitoring peptide tyrosine nitration by spectroscopic methods. *Amino Acids* **2021**, *53*, 517−532.

(69) Tuma, R. Raman spectroscopy of proteins: from peptides to large assemblies. *J. Raman Spectrosc.* **2005**, *36*, 307−319.

(70) Rygula, A.; Majzner, K.; Marzec, K. M.; Kaczor, A.; Pilarczyk, M.; Baranska, M. Raman spectroscopy of proteins: a review. *J. Raman Spectrosc.* **2013**, *44*, 1061−1076.

(71) Radi, R. Protein tyrosine nitration: biochemical mechanisms and structural basis of its functional effects. *Acc. Chem. Res.* **2013**, *46*, 550−559.

(72) Douki, T.; Cadet, J. Peroxynitrite mediated oxidation of purine bases in nucleosides and DNA. *Free Radic. Res. Commun.* **1996**, *24*, 369−380.

(73) Douki, T.; Martini, R.; Ravanat, J.-L.; Turesky, R. J.; Cadet, J. Measurement of 2,6-diamino-4-hydroxy-5-formamidopyrimidine and 8-oxo-7,8-dihydroguanine in isolated DNA exposed to gamma radiation in aqueous solution. *Carcinogenesis* **1997**, *18*, 2385−2391.

(74) Cadet, J.; Douki, T.; Ravanat, J.-L. Oxidatively generated damage to cellular DNA by UVB and UVA radiation. *Photochem. Photobiol.* **2015**, *91*, 140−155.

(75) Brown, D. J.; Evans, R. F.; Cowden, W. B.; Fenn, M. D. *The Pyrimidine*; John Wiley & Sons, Inc.: New York, USA, 1994; pp 96−106

(76) Nonoyama, N.; Oshima, H.; Shoda, C.; Suzuki, H. The reaction of peroxynitrite with organic molecules bearing a biologically important functionality. The multiplicity of reaction modes as exemplified by hydroxylation, nitration, nitrosation, dealkylation, oxygenation, and oxidative dimerization and cleavage. *Bull. Chem. Soc. Jpn.* **2001**, *74*, 2385−2395.

(77) Kamiya, H. Mutagenic potentials of damaged nucleic acids produced by reactive oxygen/nitrogen species: approaches using synthetic oligonucleotides and nucleotides. *Nucleic Acids Res.* **2003**, *31*, 517−531.

(78) McAvan, B. S.; Bowsher, L. A.; Powell, T.; O'Hara, J. F.; Spitali, M.; Goodacre, R.; Doig, A. J. Raman spectroscopy to monitor post-translational modifications and degradation in monoclonal antibody therapeutics. *Anal. Chem.* **2020**, *92*, 10381−10389.

(79) Fung, T. S.; Liu, D. X. Post-translational modifications of coronavirus proteins: roles and function. *Future Virol.* **2018**, *13*, 405−430.

(80) Nick Pace, C.; Martin Scholtz, J. A helix propensity scale based on experimental studies of peptides and proteins. *Biophys. J.* **1998**, *75*, 422−427.

(81) Colombo, G.; Meli, M.; Morra, G.; Gabizon, R.; Gasset, M. Methionine sulfoxides on prion protein helix-3 switch on the α-fold destabilization required for conversion. *PLoS One* **2009**, *4*, No. e4296.

(82) Reichmann, D.; Jakob, U. The roles of conditional disorder in redox proteins. *Curr. Opin. Struct. Biol.* **2013**, *23*, 436−442.

(83) Wouters, M. A.; Fan, S. W.; Haworth, N. L. Disulfides as redox switches: from molecular mechanisms to functional significance. *Antioxid. Redox Signaling* **2010**, *12*, 53−91.

(84) Arnesano, F.; Balatri, E.; Banci, L.; Bertini, I.; Winge, D. R. Folding studies of Cox17 reveal an important interplay of cysteine oxidation and copper binding. *Structure* **2005**, *13*, 713−722.

(85) Thompson, L. R.; Zeng, Q.; Kelly, L.; Huang, K. H.; Singer, A. U.; Stubbe, J.; Chisholm, S. W. Phage auxiliary metabolic genes and the redirection of cyanobacterial host carbon metabolism. *Proc. Natl. Acad. Sci. U.S.A.* **2011**, *108*, E757–E764.

(86) Santos, J.; Iglesias, V.; Pintado, C.; Santos-Suárez, J.; Ventura, S. DispHred: a server to predict pH-dependent order-disorder transitions in intrinsically disordered proteins. *Int. J. Mol. Sci.* **2020**, *21*, 5814.

(87) Takeuchi, H. Raman structural markers of tryptophan and histidine side chains in proteins. *Biopolymers* **2003**, *72*, 305–317.

(88) Campbell, F.; Archer, B.; Laurenson-Schafer, H.; Jinnai, Y.; Konings, F.; Batra, N.; Pavlin, B.; Vandemaele, K.; Van Kerkhove, M. D.; Jombart, T.; Morgan, O.; le Polain de Waroux, O. Increased transmissibility and global spread of SARS-CoV-2 variants of concern as at June 2021. *Euro Surveill.* **2021**, *26*, 2100509.

(89) Homma, Y.; Katsuta, T.; Oka, H.; Inoue, K.; Toyoshima, C.; Iwaki, H.; Yamashita, Y.; Shinomiya, H. The incubation period of the SARS-CoV-2 B1.1.7 variant is shorter than that of other strains. *J. Infect.* **2021**, *83*, e15–e17.

(90) Hwang, H.; Lim, J.-S.; Song, S.-A.; Achangwa, C.; Sim, W.; Kim, G.; Ryu, S. Transmission dynamics of the Delta variant of SARS-CoV-2 infections in South Korea. *J. Infect. Dis.* **2022**, *225*, 793–799.

(91) Teyssou, E.; Delagrèverie, H.; Visseaux, B.; Lambert-Niclot, S.; Brichler, S.; Ferre, V.; Marot, S.; Jary, A.; Todesco, E.; Schnuriger, A.; Ghidaoui, E.; Abdi, B.; Akhavan, S.; Houhou-Fidouh, N.; Charpentier, C.; Morand-Joubert, L.; Boutolleau, D.; Descamps, D.; Calvez, V.; Marcelin, A. G.; Soulie, C. The Delta SARS-CoV-2 variant has a higher viral load than the Beta and the historical variants in nasopharyngeal samples from newly diagnosed COVID-19 patients. *J. Infect.* **2021**, *83*, e1–e3.

(92) Walls, A. C.; Park, Y.-J.; Tortorici, M. A.; Wall, A.; McGuire, A. T.; Veesler, D. Structure, function, and antigenicity of the SARS-CoV-2 spike glycoprotein. *Cell* **2020**, *181*, 281–292.

(93) Hulswit, R. J. G.; de Haan, C. A. M.; Bosch, B.-J. Coronavirus spike protein and tropism changes. *Adv. Virus Res.* **2016**, *96*, 29–57.

(94) Li, Q.; Wu, J.; Nie, J.; Zhang, L.; Hao, H.; Liu, S.; Zhao, C.; Zhang, Q.; Liu, H.; Nie, L.; Qin, H.; Wang, M.; Lu, Q.; Li, X.; Sun, Q.; Liu, J.; Zhang, L.; Li, X.; Huang, W.; Wang, Y. The impact of mutations in SARS-CoV-2 spike on viral infectivity and antigenicity. *Cell* **2020**, *182*, 1284–1294.

(95) Zheng, J.; Yamada, Y.; Fung, T. S.; Huang, M.; Chia, R.; Liu, D. X. Identification of N-linked glycosylation sites in the spike protein and their functional impact on the replication and infectivity of coronavirus infectious bronchitis virus in cell culture. *Virol* **2018**, *513*, 65–74.

(96) Mlcochova, P.; Kemp, S. A.; Dhar, M. S.; Papa, G.; Meng, B.; Ferreira, I. A. T. M.; Datir, R.; Collier, D. A.; Albecka, A.; Singh, S.; Pandey, R.; Brown, J.; Zhou, J.; Goonawardane, N.; Mishra, S.; Whittaker, C.; Mellan, T.; Marwal, R.; Datta, M.; Sengupta, S.; Ponnusamy, K.; Radhakrishnan, V. S.; Abdullahi, A.; Charles, O.; Chattopadhyay, P.; Devi, P.; Caputo, D.; Peacock, T.; Wattal, C.; Goel, N.; Satwik, A.; Vaishya, R.; Agarwal, M.; Mavousian, A.; Lee, J. H.; Bassi, J.; Mavousian, A.; Lee, J. H.; Bassi, J.; Silacci-Fegni, C.; Saliba, C.; Pinto, D.; Irie, T.; Yoshida, I.; Hamilton, W. L.; Sato, K.; Bhatt, S.; Flaxman, S.; James, L. C.; Corti, D.; Piccoli, L.; Barclay, W. S.; Rakshit, P.; Agrawal, A.; Gupta, R. K.; The Indian SARS-CoV-2 Genomics Consortium (INSACOG); The Genotype to Phenotype Japan (G2P-Japan) Consortium; The CITIID-NIHR BioResource COVID-19 Collaboration. SARS-CoV-2 B.1.617.2 Delta variant replication and immune evasion. *Nature* **2021**, *599*, 114–119.

(97) Hristova, K.; Wimley, W. C. A look at arginine in membranes. *J. Membr. Biol.* **2011**, *239*, 49–56.

(98) Overman, S. A.; Thomas, G. J., Jr. Amide modes of the α-helix: Raman spectroscopy of filamentous virus fd containing peptide ^{13}C and ^{2}H labels in coat protein subunits. *Biochem* **1998**, *37*, 5654–5665.

(99) Nagy, P. I.; Noszál, B. Theoretical study of the tautomeric/conformational equilibrium of aspartic acid zwitterions in aqueous solution. *J. Phys. Chem. A* **2000**, *104*, 6834–6843.

(100) Wyttenbach, T.; Witt, M.; Bowers, M. T. On the stability of amino acid zwitterions in the gas phase: the influence of derivatization, proton affinity, and alkali ion addition. *J. Am. Chem. Soc.* **2000**, *122*, 3458–3464.

(101) Wyttenbach, T.; Witt, M.; Bowers, M. T. On the question of salt bridges of cationized amino acids in the gas phase: glycine and arginine. *Int. J. Mass Spectrom.* **1999**, *182–183*, 243–252.

(102) Bhunia, S.; Srivastava, S. K.; Materny, A.; Ojha, A. K. A vibrational and conformational characterization of arginine at different pH values investigated using Raman spectroscopy combined with DFT calculations. *J. Raman Spectrosc.* **2016**, *47*, 1073–1085.

(103) Aliaga, A. E.; Garrido, C.; Leyton, P.; Diaz, G.; Gomez-Jeria, J. S.; Aguayo, T.; Clavijo, E.; Campos-Vallette, M. M.; Sanchez-Cortes, S. SERS and theoretical studies of arginine. *Spectrochim. Acta, Part A* **2010**, *76*, 458–463.

(104) Arp, D. J.; Stein, L. Y. Metabolism of inorganic N compounds by ammonia-oxidizing bacteria. *Crit. Rev. Biochem. Mol. Biol.* **2003**, *38*, 471–495.

(105) Squadrito, G. L.; Pryor, W. A. The formation of peroxynitrite in vivo from nitric oxide and superoxide. *Chem.-Biol. Interact.* **1995**, *96*, 203–206.

(106) Fang, F. C. Perspectives series: host/pathogen interactions. Mechanisms of nitric oxide-related antimicrobial activity. *J. Clin. Invest.* **1997**, *99*, 2818–2825.

(107) Pezzotti, G.; Asai, T.; Adachi, T.; Ohgitani, E.; Yamamoto, T.; Kanamura, N.; Boschetto, F.; Zhu, W.; Zanocco, M.; Marin, E.; Bal, B. S.; McEntire, B. J.; Makimura, K.; Mazda, O.; Nishimura, I. Antifungal activity of polymethyl methacrylate/Si$_3$N$_4$ composites against Candida albicans. *Acta Biomater.* **2021**, *126*, 259–276.

(108) Boschetto, F.; Toyama, N.; Horiguchi, S.; Bock, R. M.; McEntire, B. J.; Adachi, T.; Marin, E.; Zhu, W.; Mazda, O.; Bal, B. S.; Pezzotti, G. In vitro antibacterial activity of oxide and non-oxide bioceramics for arthroplastic devices: II. Fourier transform infrared spectroscopy. *Analyst* **2018**, *143*, 2128–2140.

(109) Mohamed, B. M.; Verma, N. K.; Davies, A. M.; McGowan, A.; Crosbie-Staunton, K.; Prina-Mello, A.; Kelleher, D.; Botting, C. H.; Causey, C. P.; Thompson, P. R.; Pruijn, G. J.; Kisin, E. R.; Tkach, A. V.; Shvedova, A. A.; Volkov, Y. Citrullination of proteins: a common post-translational modification pathway induced by different nano-particles in vitro and in vivo. *Nanomedicine* **2012**, *7*, 1181–1195.

(110) Calabretta, P. J.; Chancellor, M. C.; Torres, C.; Abel, G. R.; Niehaus, C.; Birtwhistle, N. J.; Khouderchah, N. M.; Zemede, G. H.; Eggers, D. K. Silica as a matrix for encapsulating proteins: surface effects on protein structure assessed by circular dichroism spectroscopy. *J. Funct. Biomater.* **2012**, *3*, 514–527.

(111) Dado, G. P.; Gellman, S. H. Redox control of secondary structure in a designed peptide. *J. Am. Chem. Soc.* **1993**, *115*, 12609–12610.

(112) Pezzotti, G. Raman spectroscopy in cell biology and microbiology. *J. Raman Spectrosc.* **2021**, *52*, 2348–2443.

(113) Mazet, V.; Carteret, C.; Brie, D.; Idier, J.; Humbert, B. Background removal from spectra by designing and minimizing a non-quadratic cost function. *Chemom. Intell. Lab. Syst.* **2005**, *76*, 121–133.

(114) He, S.; Zhang, W.; Liu, L.; Huang, Y.; He, J.; Xie, W.; Wu, P.; Du, C. Baseline correction for Raman spectra using an improved asymmetric least squares method. *Anal. Methods* **2014**, *6*, 4402–4407.

(115) Cai, Y.; Yang, C.; Xu, D.; Gui, W. Baseline correction for Raman spectra using penalized spline smoothing based on vector transformation. *Anal. Methods* **2018**, *10*, 3525–3533.